

---

# FINITE-DIFFERENCE LEAST SQUARE METHODS FOR SOLVING HAMILTON-JACOBI EQUATIONS USING NEURAL NETWORKS

---

**Carlos Esteve-Yagüe\***

Department of Applied Mathematics  
and Theoretical Physics, University of Cambridge  
Cambridge, UK  
ce423@cam.ac.uk

\*Corresponding author

**Richard Tsai**

Department of Mathematics and Oden Institute  
for Computational Engineering and Sciences  
The University of Texas at Austin  
Austin, USA  
ytsai@math.utexas.edu

**Alex Massucco**

Dipartimento di Matematica, Università di Pavia,  
and Istituto Universitario di Studi Superiori (IUSS)  
Pavia, IT  
alex.massucco@iusspavia.it

## Abstract

We present a simple algorithm to approximate the viscosity solution of Hamilton-Jacobi (HJ) equations by means of an artificial deep neural network. The algorithm uses a stochastic gradient descent-based method to minimize the least square principle defined by a monotone, consistent numerical scheme. We analyze the least square principle's critical points and derive conditions that guarantee that any critical point approximates the sought viscosity solution. The use of a deep artificial neural network on a finite difference scheme lifts the restriction of conventional finite difference methods that rely on computing functions on a fixed grid. This feature makes it possible to solve HJ equations posed in higher dimensions where conventional methods are infeasible. We demonstrate the efficacy of our algorithm through numerical studies on various canonical HJ equations across different dimensions, showcasing its potential and versatility.

**Keywords** Hamilton-Jacobi equations, deep learning, finite-difference methods, least squares principle, optimal control and differential games.

**AMS subject classifications (MSC2020)** 49L25, 35A15, 68T07, 49K20, 65N06

## 1 Introduction

In recent years, significant research has focused on computing solutions for partial differential equations in high dimensions. These endeavours are driven by advancements in deep learning and new numerical optimization algorithms. In particular, there is great interest in numerical algorithms for Hamilton-Jacobi equations arising in optimal control problems and differential games.

We consider the boundary value problem associated with a Hamilton-Jacobi equation of the form

$$\begin{cases} H(x, \nabla u(x)) = 0 & x \in \Omega \\ u(x) = g(x) & x \in \partial\Omega, \end{cases} \quad (1.1)$$

where  $\Omega \subset \mathbb{R}^d$ , with  $d \geq 1$ , is an open bounded domain with Lipschitz boundary, and

$$H : \Omega \times \mathbb{R}^d \rightarrow \mathbb{R} \quad \text{and} \quad g : \partial\Omega \rightarrow \mathbb{R}$$

are the given functions, which we shall refer to as the Hamiltonian and the boundary condition, respectively. Throughout the paper, we shall assume that

$$x \mapsto g(x) \text{ is Lipschitz on } \partial\Omega \quad (1.2)$$

and

$$(x, p) \mapsto H(x, p) \text{ is locally Lipschitz in } \Omega \times \mathbb{R}^d \text{ and differentiable with respect to } p. \quad (1.3)$$

Certain types of Hamilton-Jacobi equations describe the optimality condition for an optimal control problem. By applying Bellman's dynamic programming principle, one can show that the value function of the associated optimal control problem formally satisfies the so-called Hamilton-Jacobi-Bellman equation (see [2]). However, it is well-known that even if the boundary condition  $g$  is very smooth, the boundary value problem (1.1) is not guaranteed a classical solution. This happens when the characteristics of (1.1), representing the optimal trajectories of the optimal control problem, collide with each other. On the other hand, continuous functions that satisfy the PDE for almost every  $x \in \Omega$  along with the boundary condition are not necessarily unique. In [8], Crandall and Lions introduced the notion of viscosity solution to single out a unique weak solution for the problem (1.1). Furthermore, in many situations, one can prove that the viscosity solution coincides with the value function, and one may use it to synthesize the optimal feedback for the control problem.

A characterisation of the viscosity solution can be obtained through the so-called *vanishing viscosity method*, which consists of approximating the viscosity solution by the unique classical solution to the problem

$$\begin{cases} H(x, \nabla u^\varepsilon(x)) - \varepsilon \Delta u^\varepsilon(x) = 0, & x \in \Omega, \\ u^\varepsilon(x) = g(x), & x \in \partial\Omega, \end{cases} \quad (1.4)$$

for  $\varepsilon > 0$ . The viscosity solution to (1.1) is obtained as the point-wise limit of  $u^\varepsilon(x)$  as  $\varepsilon \rightarrow 0^+$ . A different characterisation of the viscosity solution exists, using smooth test functions, which is based on the comparison principle (see [7]). Depending on the structure of the Hamiltonian and the boundary data, the viscosity solution may be discontinuous (see [2, 15]). This is typically true for Hamilton-Jacobi equations arising in differential game theory or when the boundary condition is prescribed along a characteristic curve. However, in this paper, we make the following assumption:

**Assumption 1.** *The boundary value problem (1.1) has a Lipschitz continuous viscosity solution.*

The design and implementation of numerical algorithms to approximate the viscosity solution of (1.1) is a classical problem widely considered throughout the years. In two or three dimensions, Hamilton-Jacobi equations are typically solved by special finite-difference methods operating on uniform Cartesian grids. The Hamiltonian  $H$  is approximated by a so-called numerical Hamiltonian  $\hat{H}$  defined on the grid and the grid function. If  $\hat{H}$  is *consistent* with  $H$  and *monotone* (see Definition 1), the solution to the system of discrete equations defined by  $\hat{H}$  on the grid (properly extended to the domain  $\bar{\Omega}$ ) converges uniformly to the viscosity solution as the grid spacing tends to 0 (see e.g. [9, 3]). Similar to the development of numerical schemes for hyperbolic conservation laws, higher-order approximations to the partial derivatives are proposed to be used with a monotone and consistent numerical Hamiltonian. In parallel, fast algorithms such as the fast marching methods [32, 25, 26, 14] and fast sweeping methods [36, 31] are developed for certain class of Hamilton-Jacobi equations to solve the resulting nonlinear system with computational complexities that are linear in  $N_d$ , the total number of unknowns (for the fast marching methods, the formal complexity is  $N_d \log N_d$ ).

The main drawback of finite-difference methods implemented in the classical fashion is that they involve solving a system of nonlinear equations with as many unknowns as the number of grid points. This means that the complexity of these methods scales at least exponentially with the dimension of the domain. Therefore, the classical method of formulating and solving for finite difference approximations on grid functions cannot be carried out in the high-dimensional setup. In many control theory applications, the state's dimension is large, and thence, the associated Hamilton-Jacobi-Bellman equation has to be stated in a high-dimensional domain. Recently, there has been substantial development on algorithms for solving high dimensional problems utilizing ideas from the Hopf-Lax formula and its generalization; see, e.g. [11],[6]. Other algorithms [12, 17, 13] use tensor decomposition to address special classes of high-dimensional Hamilton-Jacobi equations arising in optimal control theory.

In recent years, Deep Learning approaches have proven very effective at solving some non-linear issues in high dimensions. These methods consist on approximating a target function (in our case, the viscosity solution)

by an artificial neural network, whose parameters are optimised by minimising a loss function (typically) through a gradient-based method. This can be formulated as a variational problem of the form

$$u^* \in \arg \min_{u \in \mathcal{F}} \mathcal{J}(u), \quad (1.5)$$

where

$$\mathcal{F} := \{u(\cdot, \theta) : \theta \in \mathbb{R}^P\} \subset C(\overline{\Omega})$$

is a parameterized class of functions given by a Neural Network architecture, and  $\mathcal{J} : C(\overline{\Omega}) \rightarrow \mathbb{R}^+$  is the loss functional. Of course, the success of this method heavily relies on the choice of  $\mathcal{F}$ ,  $\mathcal{J}(\cdot)$  and the optimization algorithm.

Concerning the choice of the functional, it is necessary that  $\mathcal{J}(u)$  yields smaller values for functions  $u$  close to the target function. A common practice in Deep Learning is to seek a minimizer of  $\mathcal{J}(\cdot)$  in  $\mathcal{F}$  using information derived from  $\nabla_{\theta} \mathcal{J}(\Phi(\cdot, \theta))$ . Let us consider the following continuous version of the gradient descent method to find a minimizer of  $\mathcal{J}$  in  $\mathcal{F}$ :

$$\frac{d}{dt} \theta_t = -\nabla_{\theta} \mathcal{J}(u(\cdot, \theta_t)) = -\mathcal{J}'(u(\cdot, \theta_t)) \nabla_{\theta} u(\cdot, \theta_t), \quad (1.6)$$

where, for any continuous function  $u \in C(\overline{\Omega})$ ,  $\mathcal{J}'(u) \in C(\overline{\Omega})^*$  denotes the Fréchet derivative of  $\mathcal{J}(\cdot)$  at  $u$ , and  $\nabla_{\theta} u(\cdot, \theta)$  denotes the vector-valued function with the partial derivatives of  $u(x, \theta)$  with respect to the parameter  $\theta$ . We see that a parameter  $\theta \in \mathbb{R}^P$  is a stationary point of (1.6) if and only if all the elements of the vector  $\nabla_{\theta} u(\cdot, \theta) \in [C(\overline{\Omega})]^P$  lie in the kernel of the linear functional  $\mathcal{J}'(u(\cdot, \theta))$ . The precise form of the vector-valued function  $\nabla_{\theta} u(\cdot, \theta)$  depends on the architecture of the Neural Network and will not be discussed in this paper. On the other hand, any parameter  $\theta \in \mathbb{R}^P$  such that the function  $u = u(\cdot, \theta)$  is a solution to the Euler-Lagrange equation  $\mathcal{J}'(u) = 0$  is a critical point of  $\theta \mapsto \mathcal{J}(u(\cdot, \theta))$ , and therefore, a stationary point for the gradient descent method.

In this paper, we investigate the choice of the functional  $\mathcal{J}(\cdot)$ . Namely, we are interested in constructing a functional with the two following properties:

- i. Any global minimiser of  $\mathcal{J}(u)$  approximates the viscosity solution of (1.1).
- ii. Any critical point of  $\mathcal{J}(u)$  is a global minimizer.

Note that the second property above is crucial in Deep Learning since the optimisation algorithm used to minimise  $\mathcal{J}(u)$  is typically a variant of gradient descent, similar to (1.6). In particular, we shall look at functionals with the structure

$$\mathcal{J}(u) = \mathcal{L}(u; g) + \mathcal{R}(u),$$

where  $\mathcal{L}(u; g)$  and  $\mathcal{R}(u)$  are, respectively, fitting terms related to the boundary data  $g$ , and the PDE in (1.1). The main contribution of the current paper is to prove that if we construct  $\mathcal{R}(u)$  based on a suitable Lax-Friedrichs numerical Hamiltonian, then one can ensure that the two properties stated above hold.

We point out that there exist other variational approaches for solving Hamilton-Jacobi equations. In [20, 21], the viscosity solution of a Hamilton-Jacobi equation is identified with the saddle-point of a min-max problem, whose solution is addressed through a primal-dual hybrid gradient algorithm. In contrast, in developing our proposed formulation, we aim to benefit from the optimisation techniques commonly used in Deep Learning.

In the next section, we illustrate our findings with a simple example. In particular, we consider the Eikonal equation in a one-dimensional interval. First, we compute the optimality condition for a functional based on the PDE residual. Then, we carry out the same computation for a functional based on the residual of a finite-difference approximation of the Hamiltonian. In Section 3, we discuss existing approaches based on Deep Learning for the numerical approximation of PDEs, such as the well-known framework known as *Physics informed Neural Networks*, or PINNs. In Section 4, we study the critical points of loss functionals based on numerical Hamiltonians of Lax-Friedrichs type and present our main theoretical contributions. Section 5 is devoted to the numerical aspects of our approach. First, we describe our algorithm to approximate the viscosity solution employing a Neural Network, and then, we test our method in several examples of Hamilton-Jacobi equations. In Section 6, we present the proofs of the theoretical results presented in Section 4. Finally, we conclude the paper in Section 7, summarising our contributions and some perspectives for future research.

The code to reproduce the numerical experiments from Section 5 is publicly available in the following link:

[https://github.com/carlosesteveyague/HamiltonJacobi\\_LeastSquares\\_LxF\\_NNs](https://github.com/carlosesteveyague/HamiltonJacobi_LeastSquares_LxF_NNs)

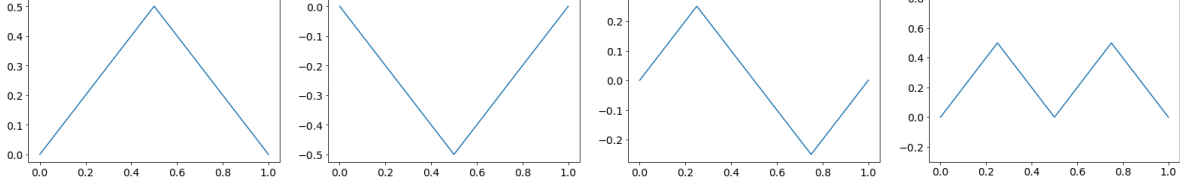


Figure 1: Four weak solutions of the Eikonal equation  $(\partial_x u)^2 - 1 = 0$  in  $\Omega := (0, 1)$  with boundary condition  $u(0) = u(1) = 0$ , corresponding to four global minimizers to the functional (3.2).

## 2 Example

Consider the model viscous Eikonal equation in the unit interval, with Dirichlet boundary conditions:

$$\begin{cases} (\partial_x u)^2 = 1 + \varepsilon \partial_{xx} u & x \in (0, 1), \\ u(0) = u_0, \quad u(1) = u_1. \end{cases} \quad (2.1)$$

It is well-known that, for any  $\varepsilon \neq 0$  and  $u_0, u_1 \in \mathbb{R}$ , the problem (2.1) has a unique  $C^\infty$ -solution.

Let us consider the minimisation problem

$$\min_u \mathcal{R}_\varepsilon(u) := \frac{1}{2} \int_0^1 ((\partial_x u(x))^2 - \varepsilon \partial_{xx} u(x) - 1)^2 dx, \quad (2.2)$$

among functions in  $C^\infty(0, 1)$  satisfying the boundary conditions  $u(0) = u_0$  and  $u(1) = u_1$ .

For any  $u \in C^\infty(0, 1)$ , let us define the PDE-residual function  $w(x) = (\partial_x u(x))^2 - \varepsilon \partial_{xx} u(x) - 1$ . For any test function  $v \in C_0^2(0, 1)$ , the Gâteaux derivative of  $\mathcal{R}_\varepsilon(\cdot)$  at  $u$  in the direction  $v$  can be written as

$$\begin{aligned} D_v \mathcal{R}_\varepsilon(u) &= \int_0^1 \underbrace{((\partial_x u)^2 - \varepsilon \partial_{xx} u - 1)}_{=w} (2\partial_x u \partial_x v - \varepsilon \partial_{xx} v) dx \\ &= -2 \int_0^1 v (\partial_x (w \partial_x u) + \varepsilon \partial_{xx} w) dx - [w(1) \partial_x v(1) - w(0) \partial_x v(0)]. \end{aligned}$$

Now, suppose that  $u^* \in C^\infty(0, 1)$  is a critical point of  $\mathcal{R}_\varepsilon(\cdot)$ . Then,  $w$  is a weak solution of

$$\begin{cases} \partial_x (w \partial_x u^*) + \varepsilon \partial_{xx} w = 0 & \text{in } (0, 1), \\ w(0) = w(1) = 0. \end{cases}$$

It is clear that, for any  $\varepsilon \neq 0$ , the unique weak solution to this boundary value problem is  $w = 0$ . Therefore any critical point  $u^* \in C^\infty(0, 1)$  of  $\mathcal{R}_\varepsilon(\cdot)$ , satisfying the boundary conditions is a classical solution of

$$(\partial_x u)^2 - \varepsilon \partial_{xx} u - 1 = 0.$$

Since this PDE, coupled with boundary conditions  $u(0) = u_0$  and  $u(1) = u_1$ , has a unique classical solution, we deduce that this solution is the unique critical point of  $\mathcal{R}_\varepsilon(\cdot)$  in  $C^\infty(0, 1)$ .

The sign of  $\varepsilon$  determines the convexity of the solution. The commonly sought-after *viscosity solution*, in this case, corresponds to the limit of the solution as  $\varepsilon \rightarrow 0^+$ , and can be proven to be concave. If we consider  $\varepsilon = 0$ , the boundary value problem (2.1) has no classical solution, so there are no critical points of  $\mathcal{R}_0(\cdot)$  in  $C^\infty(0, 1)$ . This implies, in particular, that the functional  $\mathcal{R}_0(\cdot)$  is not minimised by any smooth function. One can, however, construct minimisers of  $\mathcal{R}_0(u)$ , which are Lipschitz continuous. However, these are not unique, as illustrated in Figure 1.

Despite having proved the uniqueness of a critical point in  $C^\infty(0, 1)$  for any  $\varepsilon > 0$ , it is worth mentioning that there exist other continuous global minimizers of  $\mathcal{R}_\varepsilon(\cdot)$  which satisfy the boundary condition and are not  $C^\infty$ . Consider, for instance, the boundary value problems

$$\begin{cases} (\partial_x \phi_1)^2 = 1 + \varepsilon \partial_{xx} \phi_1 & x \in (0, 1/2), \\ \phi_1(0) = u_0, \quad \phi_1(1/2) = u_{1/2}. \end{cases} \quad \text{and} \quad \begin{cases} (\partial_x \phi_2)^2 = 1 + \varepsilon \partial_{xx} \phi_2 & x \in (1/2, 1), \\ \phi_2(1/2) = u_{1/2}, \quad \phi_2(1) = u_1, \end{cases} \quad (2.3)$$

for any  $u_{1/2} \in \mathbb{R}$ . Both problems admit a unique classical solution in  $C^\infty(0, 1/2)$  and  $C^\infty(1/2, 1)$  respectively. Note that the function

$$u(x) := \begin{cases} \phi_1(x) & x \in (0, 1/2) \\ \phi_2(x) & x \in (1/2, 1) \end{cases}$$

is continuous and minimises the functional  $\mathcal{R}_\varepsilon(\cdot)$ , since it satisfies the boundary condition and the PDE for a.e.  $x \in (0, 1)$ . This proves that the minimiser of  $\mathcal{R}_\varepsilon(\cdot)$  is not unique in the space of continuous functions. Although we could constraint the optimization to a class of  $C^\infty$  functions, this would not solve the problem due to the density of  $C^\infty(0, 1)$  in  $C(0, 1)$ . Indeed, there exist minimizing sequences of  $C^\infty$  functions converging to global minimisers of  $\mathcal{R}_\varepsilon(\cdot)$  which are not the classical solution to (2.1).

To overcome the above issues, one needs to consider a loss functional that ensures certain regularity on the minimisers and critical points. The idea of adding a diffusion term to enhance regularity and convexify the functional was exploited in [18]. There, the regularity of the solution is enhanced by adding a Sobolev norm to the functional, whereas the convexity of the functional is obtained by considering a diffusion term and a weighting function, allowing for a Carleman type inequality.

In this work, we propose a different way to enhance regularity in the functional. Namely, instead of considering functionals based on the PDE residual, we consider minimising the  $L^2$ -residual of a finite-difference numerical scheme. For any  $N \in \mathbb{N}$ , set  $\delta := 1/N$ , the uniform grid  $\bar{\Omega}_\delta := \delta\mathbb{Z} \cap [0, 1]$ , and consider the following discrete version of the PDE-residual functional  $\mathcal{R}_\varepsilon(\cdot)$  defined in (2.2), with  $\varepsilon = 0$ :

$$\min_u \widehat{\mathcal{R}}(u) := F(U) = \sum_{i=1}^{N-1} \delta \left[ \widehat{H}_\alpha \left( \frac{u_{i+1} - u_i}{\delta}, \frac{u_i - u_{i-1}}{\delta} \right) \right]^2, \quad \text{subject to } u_0 = u_N = 0, \quad (2.4)$$

where, for any  $u \in C([0, 1])$ , the vector  $U := (u_0, \dots, u_N) \in \mathbb{R}^{N+1}$  is the grid function on  $\bar{\Omega}_\delta$  associated to  $u$ , and

$$\widehat{H}_\alpha(p^+, p^-) = \left( \frac{p^+ + p^-}{2} \right)^2 - \alpha \frac{p^+ - p^-}{2} - 1$$

for some  $\alpha > 0$ , is the Lax-Friedrichs numerical Hamiltonian associated to  $H(p) = p^2 - 1$ .

Note that the functional  $F(\cdot)$  is differentiable in  $\mathbb{R}^{N+1}$ , and then, the grid function  $U \in \mathbb{R}^{N+1}$  associated to any local minimizer  $u \in C([0, 1])$  must satisfy the first-order optimality condition  $\nabla F(U) = 0$ .

Denoting  $p_i^\pm = \pm(u_{i\pm 1} - u_i)/\delta$ , we can write the partial derivative of  $F(U)$  with respect to  $u_i$  as

$$\partial_{u_i} F(U) = \widehat{H}_\alpha(p_{i-1}^+, p_{i-1}^-) (p_{i-1}^+ + p_{i-1}^- - \alpha) - \widehat{H}_\alpha(p_{i+1}^+, p_{i+1}^-) (p_{i+1}^+ + p_{i+1}^- + \alpha) + 2\alpha \widehat{H}_\alpha(p_i^+, p_i^-),$$

for any  $i = 2, \dots, N-2$ .

Now, let us denote

$$w_i = \widehat{H}_\alpha(p_i^+, p_i^-) \quad \text{and} \quad v_i = p_i^+ + p_i^-, \quad \text{for } i = 1, \dots, N-1.$$

Using this notation, we can write the optimality condition for  $u_i$  with  $i = 2, \dots, N-2$  as

$$-(\alpha - v_{i-1})w_{i-1} - (\alpha + v_{i+1})w_{i+1} + 2\alpha w_i = 0, \quad i = 2, \dots, N-2.$$

Further, since

$$\begin{aligned} \partial_{u_1} F(U) &= 2\alpha \widehat{H}_\alpha(p_1^+, p_1^-) - \widehat{H}_\alpha(p_2^+, p_2^-)(p_2^+ + p_2^- + \alpha) \\ &= -(\alpha + v_2)w_2 + 2\alpha w_1, \\ \partial_{u_{N-1}} F(U) &= \widehat{H}_\alpha(p_{N-2}^+, p_{N-2}^-)(p_{N-2}^+ + p_{N-2}^- - \alpha) + 2\alpha \widehat{H}_\alpha(p_{N-1}^+, p_{N-1}^-) \\ &= -(\alpha - v_{N-2})w_{N-2} + 2\alpha w_{N-1}, \end{aligned}$$

we obtain the first-order optimality condition for the minimization problem (2.4), which reads as

$$\begin{cases} -v_2 w_2 - \alpha(w_2 - 2w_1) = 0 \\ v_{i-1} w_{i-1} - v_{i+1} w_{i+1} - \alpha(w_{i+1} + w_{i-1} - 2w_i) = 0 \quad \text{for } i = 2, \dots, N-2 \\ v_{N-2} w_{N-2} - \alpha(w_{N-2} - 2w_{N-1}) = 0. \end{cases} \quad (2.5)$$

Denoting  $W = (w_1, \dots, w_{N-1})$  and  $V = (v_1, \dots, v_{N-1})$ , this system of equations can be written as

$$-(A_N(V) + \alpha \Delta_N)W = 0, \quad (2.6)$$

where  $A_N(V) \in \mathbb{R}^{(N-1) \times (N-1)}$  is a matrix depending on  $V$  and  $\Delta_N \in \mathbb{R}^{(N-1) \times (N-1)}$  is the Toeplitz matrix associated to the discrete Laplace operator on a uniform grid with  $N-1$  points. It turns out that, for  $\alpha$  and  $\delta = 1/N$  sufficiently big, the matrix  $A_N(V) + \alpha \Delta_N$  is negative definite, which implies that the optimality system (2.6) has only the trivial solution  $W = 0$ . This implies that, if  $u$  is a critical point of  $\widehat{\mathcal{R}}(\cdot)$ , then the associated grid function  $U = (u_0, \dots, u_N)$  satisfies

$$w_i = \left( \frac{u_{i+1} - u_{i-1}}{2\delta} \right)^2 - \alpha \frac{u_{i+1} + u_{i-1} - 2u_i}{2\delta} - 1 = 0, \quad \text{for all } i = 1, \dots, N-1. \quad (2.7)$$

In other words,  $U$  satisfies the finite-difference equation associated with the Lax-Friedrichs numerical Hamiltonian  $\widehat{H}_\alpha(p^+, p^-)$ . See Section 4 for the precise estimates on  $\alpha$  and  $\delta$ , and Section 6 for the precise computations in the multi-dimensional setup. For  $\alpha$  sufficiently large, one can prove that the numerical Hamiltonian  $\widehat{H}_\alpha(p^+, p^-)$  is consistent with  $H(p) = p^2$  and monotone, as per Definition 1. Moreover, it is known (see [9, 3]) that finite-difference solutions for consistent and monotone numerical schemes converge to the viscosity solution as  $\delta \rightarrow 0^+$ . In Section 5, we propose a strategy to train a Neural Network, first with a large value of  $\delta$ , ensuring that any critical point solves the equation 2.7, and then progressively reducing  $\delta$  to ensure convergence to the viscosity solution.

Of course, in the multi-dimensional case, a functional such as  $\widehat{\mathcal{R}}(u)$  in (2.4) would involve a summation over a multidimensional grid. Computing the full gradient of  $\widehat{\mathcal{R}}(u)$  would be computationally infeasible. However, in practice, one can use a version of stochastic gradient descent, in which at every gradient step, the gradient of  $\widehat{\mathcal{R}}(u)$  is approximated by the gradient of a randomized selection of the terms in the sum.

### 3 Deep Learning and Partial Differential Equations

Due to its tremendous success in fields such as computer graphics and computer vision, Deep Learning has recently become a popular candidate for tackling various problems where classical methods face limitations. These include the numerical approximation of PDEs in multiple settings. Under the Deep Learning framework, one typically minimizes a functional  $\mathcal{J} : C(\Omega) \rightarrow \mathbb{R}^+$ ,

$$u \in \arg \min_{u \in \mathcal{F}} \mathcal{J}(u), \quad (3.1)$$

where  $\mathcal{F} \subset C(\overline{\Omega})$  is a class of functions defined by a neural network architecture. If  $\mathcal{J}(u) \equiv J(u; D)$  is based on some notion of misfit between the minimiser  $u$  and a given data set  $D$ , the setup is often called “supervised learning” in the machine learning community. If  $\mathcal{J}$  is defined without using data, the setup is often called “unsupervised”.

One of the reasons for the success of Deep Learning techniques comes from the fact that the commonly used (deep) neural networks can be constructed to approximate continuous functions in high dimensions conveniently [4, 35, 28] and very efficiently for certain classes of smooth functions [1, 29, 30, 34, 33].

Another reason for the success of Deep Learning techniques is the development of optimisation methods, which are used to address the problem (3.1). These are generally gradient-based iterative methods, such as stochastic gradient descent or variants thereof. Hence, the choice of the functional  $\mathcal{J}(u)$  becomes of utmost importance. For finding the viscosity solution to the boundary value problem (1.1), we consider loss functionals of the form

$$\mathcal{J}(u) = \mathcal{L}(u; D) + \mathcal{R}(u).$$

In [23], the popular Deep Learning framework known as Physics Informed Neural Networks (PINNs) is introduced. In a PINNs approach,  $\mathcal{R}$  can be interpreted as a Monte-Carlo approximation of the squared  $L^2$ -norm of the PDE residual, and  $\mathcal{L}$  may involve both boundary data and possibly additional “collocation” points (pointwise values of the solution in  $\Omega$ ). When the data fitting term  $\mathcal{L}$  is present,  $\mathcal{R}$  is regarded as a regularisation term to some practitioners.

Following the PINNs strategy, a least-square principle for the Hamilton-Jacobi equation would involve

$$\mathcal{R}(u) = \int_{\Omega} H(x, \nabla u(x))^2 dx. \quad (3.2)$$

Assuming that we do not have, in principle, access to the viscosity solution in the interior of the domain, the functional  $\mathcal{L}$  can only involve the boundary data:

$$\mathcal{L}(u; g) = \int_{\partial\Omega} (u(x) - g(x))^2 dx. \quad (3.3)$$

In practice, both terms  $\mathcal{R}(u)$  and  $\mathcal{L}(u; g)$  are approximated through Monte Carlo integration.

We see that any Lipschitz continuous function  $u$  satisfying  $H(x, \nabla u(x)) = 0$  for almost every  $x \in \Omega$ , together with the boundary condition  $u(x) = g(x)$  on  $\partial\Omega$ , is a global minimizer of  $\mathcal{J}(u)$ . It is well-known that solutions of this type are not unique. This is true even for the simple Eikonal equation on a one-dimensional interval shown in Example 1. This is, of course, very inconvenient since one cannot guarantee by any means that minimizing the PINNs functional  $\mathcal{J}(u)$  with (3.2) and (3.3) would produce an approximation of the viscosity solution. See Figure 1 for an illustration of four global minimizers of the PINNs functional associated with the one-dimensional Eikonal equation in  $(0, 1)$  with zero-boundary condition. To overcome the issue of non-uniqueness of minimisers, and promote convergence to the viscosity solution, we need to modify the functional in a way that functions with certain regularity properties are enhanced. In Deep Learning, a typical technique to achieve this is to add a *regularisation* term to the functional in the form of some Sobolev norm. However, this is not the only way to enhance regularity on the minimisers. In this paper, we replace the  $L^2$ -norm of the PDE-residual by the least-square principle associated to a finite-difference numerical scheme. We prove that the numerical diffusion of the finite-difference scheme enhances regularity on the minimisers. Moreover, by choosing a suitable consistent and monotone numerical scheme, we can prove that the unique minimiser approximates the viscosity solution.

There are also supervised Deep Learning approaches to address Hamilton-Jacobi equations. Different Deep Learning approaches for learning, through data, a weak solution of Hamilton-Jacobi equations are proposed in [10] and in [5]. In [10], data is generated by numerically evolving the Hamiltonian system (the characteristic equations of the Hamilton-Jacobi equation) in the phase space, and a least square principle is used to assign the solution gradient. However, it is unclear if the minimiser is the viscosity solution. In [5], the issue of non-uniqueness of minimisers of the PDE-residual arising in Hamilton-Jacobi equations is alleviated by pre-training the NN with supervised data. In contrast, our approach requires no supervised data for convergence to the viscosity solution.

### 3.1 Why finite-difference approximations?

**Larger domain of dependence/influence.** Finite difference discretizations lead to a larger domain of dependence/influence per collocation point, compared to pointwise evaluation of the PDE residual. This feature can lead to a stronger coupling of the “pointwise losses” and to more efficient capturing of the problem’s underlying causality. This is essential as typical solutions of the HJ are not classical, and the singular sets of the solutions are lower dimensional; i.e. the probability of a finite set of collocation points “sampling” the singular set is proportional to the size of the domain of dependence of the residual term to be minimized. As a matter of fact, we show in our numerical experiments in Section 5 that reducing the discretization step does not always lead to a more accurate approximation of the solution. Indeed, our numerical experiments suggest that using a finer discretization of the PDE in the loss functional requires a larger number of collocation points during the optimisation algorithm. Evaluating the PDE residual at the collocation points would be equivalent to letting the discretization step go to zero, which would result in a dramatic increase on the number of collocation points needed to effectively compute the solution.

**Simpler loss gradient evaluations.** While automatic differentiation can be a very convenient and efficient tool for evaluating first-order derivatives, the evaluation of second-order derivatives can be costly with a large memory footprint. See e.g. [27] and [19], Tab. V.

**Convergence to the viscosity solutions.** By using a convergent monotone numerical scheme, e.g. [9], our proposed algorithm is capable of computing the viscosity solution of the given boundary value problem, without explicitly determining the convexity of the solution or where the characteristics of problems should collide.

## 4 Finite difference residual functionals

Let us consider a numerical Hamiltonian

$$\widehat{H}(x, p^+, p^-) : \Omega \times \mathbb{R}^d \times \mathbb{R}^d \longrightarrow \mathbb{R}.$$

For a fixed  $\delta > 0$ , we use the notation

$$D_\delta^+ u(x) := \left( \frac{u(x + \delta e_1) - u(x)}{\delta}, \dots, \frac{u(x + \delta e_d) - u(x)}{\delta} \right) \in \mathbb{R}^d$$

and

$$D_\delta^- u(x) := \left( \frac{u(x) - u(x - \delta e_1)}{\delta}, \dots, \frac{u(x) - u(x - \delta e_d)}{\delta} \right) \in \mathbb{R}^d,$$

respectively for the upwind and downwind finite-difference approximation of the gradient  $\nabla u(x)$ . Here, the vectors  $\{e_i\}_{i=1}^d$  represent the canonical basis of  $\mathbb{R}^d$ . An important definition is in order:

**Definition 1.** (*Consistency and monotonicity*)

i. We say that the numerical Hamiltonian  $\widehat{H}(x, p^+, p^-)$  is consistent if  $\widehat{H}(x, p, p) \equiv H(x, p)$ ,  $p \in \mathbb{R}^d$ .

ii. We say that the numerical Hamiltonian  $\widehat{H}(x, p^+, p^-)$  is monotone in  $\Omega$  if the function

$$(u(x), \{u(x + \delta e_i)\}_{i=1}^d, \{u(x - \delta e_i)\}_{i=1}^d) \longmapsto \widehat{H}(x, D_\delta^+ u(x), D_\delta^- u(x))$$

is non-decreasing with respect to  $u(x)$  and non-increasing with respect to  $u(x + \delta e_i)$  and  $u(x - \delta e_i)$ .

### The Lax-Friedrichs scheme

In this paper, we work with the Lax-Friedrichs scheme, given by

$$\widehat{H}_\alpha(x, p^+, p^-) := H\left(x, \frac{p^+ + p^-}{2}\right) - \alpha \sum_{i=1}^d \frac{p_i^+ - p_i^-}{2}, \quad \text{for } \alpha > 0. \quad (4.1)$$

This numerical scheme is consistent with  $H(x, p)$ , and for any  $L > 0$ , if one takes  $\alpha$  satisfying

$$\alpha \geq C_H(L) := \max_{\substack{\|p\| \leq L \\ x \in \overline{\Omega}}} \|\nabla_p H(x, p)\|, \quad (4.2)$$

then  $\widehat{H}_\alpha(x, p^+, p^-)$  is monotone at any function  $u$  with Lipschitz constant  $L$ .

For any  $\delta > 0$ , let us define the uniform grid

$$\Omega_\delta := \delta \mathbb{Z}^d \cap \Omega,$$

and consider the loss functional

$$\widehat{\mathcal{R}}(u) := \delta^d \sum_{x \in \Omega_\delta} \left[ \widehat{H}_\alpha(x, D_\delta^+ u(x), D_\delta^- u(x)) \right]^2. \quad (4.3)$$

### Global minimisers

We note that a function  $u \in C(\overline{\Omega})$  is a global minimiser of  $\widehat{\mathcal{R}}(u)$  if and only if

$$\widehat{H}_\alpha(x, D_\delta^+ u(x), D_\delta^- u(x)) = 0 \quad x \in \Omega_\delta. \quad (4.4)$$

In other words,  $u$  is a global minimiser of  $\widehat{\mathcal{R}}(u)$  if and only if the restriction of  $u$  to  $\Omega_\delta$  solves the discrete equation associated with the numerical Hamiltonian  $\widehat{H}_\alpha$ .

If  $\widehat{H}_\alpha$  is consistent with  $H$  and monotone, one can ensure (see [9, 3]) that any minimiser of  $\widehat{\mathcal{R}}(u)$  approximates a viscosity solution of the Hamilton-Jacobi equation

$$H(x, \nabla u) = 0, \quad \text{in } \Omega, \quad (4.5)$$



in the following sense: for any decreasing sequence  $\{\delta_n\}_{n \geq 1}$  with  $\delta_n \rightarrow 0^+$ , and an equicontinuous sequence of functions  $u_n \in C(\overline{\Omega})$ , each of them minimising  $\widehat{\mathcal{R}}(u)$  defined on  $\Omega_{\delta_n}$ . If  $u_n$  converge point-wise to some function  $u^* \in C(\overline{\Omega})$ , then  $u^*$  is a viscosity solution of (4.5).

With the above observation, we accomplished the first requirement for the functional  $\mathcal{R}(\cdot)$ , i.e. minimisers approximate viscosity solutions to Hamilton-Jacobi equation in (1.1). The second requirement is more subtle and is the main contribution of this paper. Namely, we provide sufficient conditions on the numerical Hamiltonian  $\widehat{H}_\alpha(x, p^+, p^-)$  and on the grid spacing  $\delta$ , ensuring that any critical point of the functional  $\widehat{\mathcal{R}}(u)$  defined in (4.3) is indeed a global minimiser. Hence, it approximates a viscosity solution of (4.5).

### Critical points

Let  $N_\delta$  denote the number of grid nodes in  $\Omega_\delta$ . For any  $u \in C(\overline{\Omega})$ , let  $U := u|_{\Omega_\delta} \in \mathbb{R}^{N_\delta}$  denote the vector corresponding to the values of  $u$  on  $\Omega_\delta$  following a chosen ordering of the grid nodes in  $\Omega_\delta$ . We define the functional  $F : \mathbb{R}^{N_\delta} \mapsto \mathbb{R}$ , given by

$$F(U) := \widehat{\mathcal{R}}(u) \quad \text{for any } u \in C(\overline{\Omega}) \text{ such that } U = u|_{\Omega_\delta}.$$

In view of (1.3), the function  $F(\cdot)$  is differentiable in  $\mathbb{R}^{N_\delta}$ , and we denote its gradient by  $\nabla F(U) \in \mathbb{R}^{N_\delta}$ .

Then, the Fréchet differential of  $\widehat{\mathcal{R}}(\cdot)$  at any  $u \in C(\overline{\Omega})$  can be written as the linear functional on  $C(\overline{\Omega})$  given by

$$\phi \in C(\overline{\Omega}) \mapsto \Phi \cdot \nabla F(U), \quad \text{where } \Phi := \phi|_{\Omega_\delta} \in \mathbb{R}^{N_\delta}.$$

Let us define the residual function  $w \in C(\overline{\Omega})$  associated to  $u$  and  $\widehat{H}_\alpha$  as

$$w(x) = \widehat{H}_\alpha(x, D_\delta^+ u(x), D_\delta^- u(x)), \quad \forall u \in C(\overline{\Omega}).$$

From the form of  $\widehat{\mathcal{R}}(u)$  in (4.3), which is a least-squares like functional, the gradient of  $F$  has the following form

$$\nabla F(U) = A_{\alpha, \delta}(U)W, \tag{4.6}$$

where  $W := w|_{\Omega_\delta} \in \mathbb{R}^{N_\delta}$ , and  $A_{\alpha, \delta}(U)$  is a linear bounded operator  $\mathbb{R}^{N_\delta} \rightarrow \mathbb{R}^{N_\delta}$ , depending on  $\widehat{H}_\alpha$  and  $U$  (see Section 6 for the explicit form). Then, for any  $u \in C(\overline{\Omega})$  critical point of  $\widehat{\mathcal{R}}(\cdot)$ , the vector of residuals  $W$  satisfies the equation

$$A_{\alpha, \delta}(U)W = 0. \tag{4.7}$$

This linear system can be seen as a finite-difference equation for the residual function  $w(x)$  on the grid  $\Omega_\delta$ . It can be interpreted as the adjoint equation associated with the finite difference system (4.4). Our next goal is to prove that by choosing suitable parameters  $\alpha$  and  $\delta$  in the numerical Hamiltonian, one can ensure that the adjoint equation (4.7) has a unique solution, which is the trivial solution  $W = 0$ . This implies that any critical point of  $\widehat{\mathcal{R}}(u)$  solves the finite-difference equation (4.4).

### 4.1 The main results

In the following theorem, for any constant  $L > 0$ , we give a sufficient condition on  $\alpha$  and  $\delta$  ensuring that any critical point  $u$  of  $\widehat{\mathcal{R}}(u)$  with Lipschitz constant  $L$  solves the finite-difference equation (4.4). We consider the domain  $\Omega$  to be a  $d$ -dimensional cube for simplicity. The result can be adapted to more general domains, satisfying suitable regularity properties, albeit with some additional technicalities.

**Theorem 1.** *Let  $H$  be a Hamiltonian satisfying (1.3), and let  $\Omega = (0, 1)^d$ ,  $d \in \mathbb{N}$ . For any fixed  $\alpha > 0$  and  $N \in \mathbb{N}$ , set  $\delta = 1/N$  and consider the uniform Cartesian grid  $\Omega_\delta := \delta \mathbb{Z}^d \cap \Omega$  and the functional  $\widehat{\mathcal{R}}(\cdot)$  defined in (4.3).*

*Let  $u \in C(\overline{\Omega})$  be a critical point of  $\widehat{\mathcal{R}}(\cdot)$  with a Lipschitz constant  $L$ . If*

$$2\alpha \sin^2\left(\frac{\pi}{2}\delta\right) > \max_{\substack{\|p\| \leq L \\ x \in \overline{\Omega}}} \|\nabla_p H(x, p)\| \tag{4.8}$$

*then*

$$\widehat{H}_\alpha(x, D_\delta^+ u(x), D_\delta^- u(x)) = 0, \quad \forall x \in \Omega_\delta. \tag{4.9}$$

The proof is given in Section 6. Essentially, it shows that if  $\alpha, \delta$  and  $L$  satisfy (4.8), then the linear operator  $A_{\alpha, \delta}(U)$  in (4.6) associated to  $\hat{H}_\alpha$  is invertible for any function  $u$  with Lipschitz constant equal or smaller than  $L$ . This implies that if the first-order optimality condition (4.7) holds, then the residuals  $W$  associated with the function  $u$  on  $\Omega_\delta$  satisfy  $W = 0$ , and hence,  $u$  solves the system of equations (4.9).

**Remark 1.** Condition (4.8) can be written as

$$\alpha \frac{\lambda_1(\Omega_\delta)}{2d} > \max_{\substack{\|p\| \leq L \\ x \in \bar{\Omega}}} \|\nabla_p H(x, p)\|,$$

where  $\lambda_1(\Omega_\delta)$  is the smallest eigenvalue of the matrix associated with the discrete Dirichlet Laplacian on the computational domain  $\Omega_\delta = \delta\mathbb{Z} \cap \Omega$ . A similar result to Theorem 1 can be proved for a more general class of domains  $\Omega$  satisfying suitable regularity conditions. However, we have restricted ourselves to the case of a  $d$ -dimensional cube for the sake of clarity of the arguments.

Since our goal is to use an artificial neural network to approximate the solution of a given Hamilton-Jacobi problem, we do not need to commit ourselves to one fixed grid as in a standard finite difference method. Therefore, we consider the functional  $\mathcal{R}(\cdot) : C(\bar{\Omega}) \rightarrow \mathbb{R}^+$  given by

$$\mathcal{R}(u) = \int_{\Omega} \left[ \hat{H}_\alpha(x, D_\delta^+ u(x), D_\delta^- u(x)) \right]^2 dx. \quad (4.10)$$

Note that

$$\mathcal{R}(u) = \int_{(0, \delta)^d} \hat{\mathcal{R}}(u; z) dz,$$

where  $\hat{\mathcal{R}}(u; z)$  is a discrete functional similar to (4.3), but on the shifted grid  $\Omega_\delta(z) := (\delta\mathbb{Z}^d + z) \cap \Omega$  for  $z \in (0, \delta)^d$ .

By minimising  $\mathcal{R}(\cdot)$ , one solves the associated finite-difference equation on a family of shifted Cartesian grids, covering the entire domain  $\Omega$  (instead of on a fixed grid). This fact is then exploited in Algorithm 2, which minimizes  $\mathcal{R}(u)$  for a decreasing sequence of  $\delta$ .

For the functional  $\mathcal{R}(u)$ , we have the following result.

**Theorem 2.** Let  $H$  be a Hamiltonian satisfying (1.3), and let  $\Omega = (0, 1)^d$ ,  $d \in \mathbb{N}$ . For any fixed  $\alpha > 0$  and  $N \in \mathbb{N}$ , set  $\delta = 1/(N - 1)$  and consider the functional  $\mathcal{R}(\cdot)$  defined in (4.10).

Let  $u \in C(\bar{\Omega})$  be any critical point of  $\mathcal{R}(\cdot)$  with a Lipschitz constant  $L$ . If (4.8) holds, then

$$\hat{H}_\alpha(x, D_\delta^+ u(x), D_\delta^- u(x)) = 0, \quad \forall x \in \Omega. \quad (4.11)$$

The proof is given in Section 6.3.

We make the following remarks concerning the above results:

- i. It is worth noting that Theorems 1 and 2 are local results in the sense that they only ensure that a critical point  $u \in C(\bar{\Omega})$  of  $\hat{\mathcal{R}}(\cdot)$  solves the finite-difference equation (4.9), provided that the Lipschitz constant of  $u$  is smaller or equal than  $L$ . It does not rule out the existence of critical points with larger Lipschitz constants that do not satisfy (4.9). However, one can take  $L > 0$  as large as needed, at the expense of increasing  $\alpha$  and  $\delta$  in such a way that (4.8) holds.
- ii. Choosing large values for  $\alpha$  and  $\delta$  has the drawback of introducing a lot of numerical diffusion, which implies that minimisers of  $\hat{\mathcal{R}}(\cdot)$  (resp.  $\mathcal{R}(\cdot)$ ) are over-regularised approximations of the actual viscosity solution. Since we want to use an iterative gradient-based method to minimise the functional (as it is typically done in Deep Learning), we must choose large values of  $\alpha$  and  $\delta$  to ensure global convergence to the minimiser. This, of course, is undesirable as the minimiser will be over-smoothed. As we explain in Section 5, and will be observed in the numerical experiments, a possible strategy to attain a global minimiser for  $\alpha$  and  $\delta$  small is to sequentially decrease the values of  $\alpha$  and  $\delta$  throughout the gradient iterations.
- iii. In Theorem 2,  $\delta = 1/(N - 1)$ , as opposed to  $\delta = 1/N$  in Theorem 1. This difference is only technical. If  $\delta = 1/N$ , then the grid  $\Omega_\delta = \delta\mathbb{Z}^d \cap \Omega$  contains  $(N - 1)^d$  points, whereas for any  $z \in (0, \delta)^d$ , the shifted grid  $\Omega_\delta(z) = (\delta\mathbb{Z}^d + z) \cap \Omega$  has  $N^d$  points. If  $\delta = 1/(N - 1)$ , then the grid  $\Omega_\delta(z)$  has  $(N - 1)^d$  points, and thus one can use the same condition (4.8) from Theorem 1.

#### 4.2 The least square principle involving a numerical Hamiltonian and supervised data

In the above section, we discussed functionals involving a numerical Hamiltonian. We show that under appropriate conditions, any global minimiser approximates a viscosity solution of the Hamilton Jacobi equation

$$H(x, \nabla u) = 0, \quad \text{in } \Omega. \quad (4.12)$$

The uniqueness of the viscosity solution to the partial differential equation (4.12) typically involves additional (suitable) boundary conditions. Likewise, our ultimate least square formulation has to incorporate boundary data.

For simplicity, consider  $\Omega = (0, 1)^d$  and functionals defined on the uniform Cartesian grid  $\bar{\Omega}_\delta := \delta\mathbb{Z}^d \cap \bar{\Omega}$ , where  $\delta = 1/N$  for some  $N \in \mathbb{N}$ . Recall that we denote the interior points of the numerical domain by  $\Omega_\delta := \delta\mathbb{Z}^d \cap \Omega$ . Similarly, we define the numerical boundary as

$$\partial\Omega_\delta := \delta\mathbb{Z}^d \cap \partial\Omega.$$

Note that  $\partial\Omega_\delta$  has to be redefined appropriately for more general domains.

For the parameters  $\alpha, \gamma > 0$ , we define the functional

$$\hat{\mathcal{J}}(u) := \delta^d \sum_{x \in \Omega_\delta} \left[ \hat{H}_\alpha(x, D_\delta^+ u(x), D_\delta^- u(x)) \right]^2 + \gamma \delta^{d-1} \sum_{x \in \partial\Omega_\delta} (u(x) - g(x))^2, \quad (4.13)$$

where  $\hat{H}_\alpha$  is the Lax-Friedrichs numerical Hamiltonian defined in (4.1) and  $g$  is the boundary condition in (1.1). The following result is a consequence of Theorem 1.

**Corollary 1.** *Let  $H$  be a Hamiltonian satisfying (1.3),  $\Omega = (0, 1)^d$ ,  $d \in \mathbb{N}$ , and  $g \in C(\partial\Omega)$ . For any  $N \in \mathbb{N}$ , set  $\delta = 1/N$  and consider the uniform Cartesian grid  $\Omega_\delta := \delta\mathbb{Z}^d \cap \Omega$  with the associated numerical boundary  $\partial\Omega_\delta := \delta\mathbb{Z}^d \cap \partial\Omega$ . For the parameters  $\alpha, \gamma > 0$ , consider the functional  $\hat{\mathcal{J}}(\cdot)$  defined in (4.13). Let  $u \in C(\bar{\Omega})$  be any critical point of  $\hat{\mathcal{J}}(\cdot)$  with Lipschitz constant  $L$ . If (4.8) holds, then*

$$\begin{cases} \hat{H}_\alpha(x, D_\delta^+ u(x), D_\delta^- u(x)) = 0, & x \in \Omega_\delta, \\ u(x) = g(x), & x \in \partial\Omega_\delta. \end{cases} \quad (4.14)$$

The proof of this corollary can be found in Section 6.2. Under the Assumption 1, and choosing  $\alpha > 0$  such that the numerical Hamiltonian  $\hat{H}_\alpha$  is monotone, Corollary 1 can be used in the following way: if one is able to construct an equicontinuous sequence  $u_n \in C(\bar{\Omega})$  minimising the functional  $\hat{\mathcal{J}}(\cdot)$ , with  $\delta_n \rightarrow 0^+$ , then  $u_n(x) \rightarrow u^*(x)$  uniformly in  $\Omega$ , where  $u^*$  is the unique viscosity solution to (1.1). Of course, it is important to note that condition (4.8) only holds if  $\delta$  is large enough. As we will see in Section 5, one can start by training a neural network with a large value of  $\delta$ , ensuring that any critical point satisfies (4.14), and then re-train the neural network with decreasing values of  $\delta$ .

A similar result holds for more general domains  $\Omega \subset \mathbb{R}^d$ , and considering the functional

$$\mathcal{J}(u) := \int_{\Omega} \left[ \hat{H}_\alpha(x, D_\delta^+ u(x), D_\delta^- u(x)) \right]^2 d\rho(x) + \gamma \int_{\partial\Omega} (u(x) - g(x))^2 d\mu(x),$$

where  $\rho$  and  $\mu$  are probability measures on  $\Omega$  and  $\partial\Omega$  respectively.

In this paper, we propose to minimize such least square principle via a stochastic gradient descent algorithm. This means that the integrals will be approximated by the Monte Carlo method. The involvement of the Monte-Carlo method requires deciding on a probability distribution  $\rho$  over  $\Omega$ , and the choice of this distribution can depend on the error metric of choice. Finally, in many applications, such as finding the shortest path to the target region, one also has data on  $\Gamma$  that rests in the interior of  $\Omega$ . Therefore, we propose a more general form of the least square principle as follows:

$$\mathcal{J}(u) := \int_{\Omega} \left[ \hat{H}_\alpha(x, D_\delta^+ u(x), D_\delta^- u(x)) \right]^2 d\rho(x) + \gamma_1 \int_{\partial\Omega} [u(x) - g(x)]^2 d\mu(x) + \gamma_2 \int_{\Gamma} [u(x) - h(x)]^2 d\nu(x), \quad (4.15)$$

where  $\rho$  is a probability measure on  $\Omega$ ,  $\mu$  and  $\nu$  are probability measures on  $\partial\Omega$  and  $\Gamma$ . In Section 5.1, we propose two simple stochastic gradient descent algorithms for minimizing  $\mathcal{J}(u)$ . Section 5.2.1 presents a study on the choice of  $\rho$  using two different metrics.

**Hyper-parameters  $\alpha$  and  $\delta$  influenced by supervised data** Using our results in Theorems 1 and 2 and Corollary 1, we can deduce that adding supervised data in the functional allows the use of a numerical Hamiltonian with less numerical diffusion, while still ensuring that any critical point of  $\mathcal{J}(\cdot)$  satisfies (4.14). Indeed, the set  $\Gamma$  can be seen as part of the boundary of an auxiliary domain  $\Omega^* := \Omega \setminus \Gamma$ . For a fixed  $\delta > 0$ , the computational grid  $\Omega_\delta^* := \delta\mathbb{Z} \cap \Omega^*$  is then a subset of the original grid  $\Omega_\delta := \delta\mathbb{Z} \cap \Omega$ , which implies that the smallest eigenvalue of the discrete Dirichlet Laplacian on  $\Omega_\delta^*$  is larger than the one on  $\Omega_\delta$ . Then, in view of Remark 1, it follows that one is allowed to take smaller values of  $\alpha$ , or  $\delta$ , while the conclusion of Theorem 1 (resp. Theorem 2 or Corollary 1) still holds. Being able to choose smaller values of  $\alpha$  and  $\delta$  reduces the numerical diffusion of the solution of (4.14), which in turn implies that the minimiser of  $\mathcal{J}(u)$  provides a more accurate approximation of the viscosity solution.

### 4.3 Uniqueness of a critical point by regularization of the Hamiltonian

In Theorem 1 (resp. Theorem 2), we provide a sufficient condition on the choice of the parameters  $\alpha$  and  $\delta$ , ensuring that any critical point of the functional  $\widehat{\mathcal{R}}(u)$  (resp.  $\mathcal{R}(u)$ ) satisfies

$$\widehat{H}_\alpha(x, D_\delta^+ u(x), D_\delta^- u(x)) = 0, \quad \forall x \in \Omega_\delta \text{ (resp. } \Omega). \quad (4.16)$$

This condition (see (4.8)) involves taking  $\alpha$  and  $\delta$  sufficiently large so that the system of equations associated with the first-order optimality condition, which is of the form  $A_{\alpha,\delta}(U)W = 0$ , admits a unique solution, i.e. the trivial solution  $W = 0$ . See Section 6 for further details.

An alternative way to ensure that any critical point of the functional solves the finite-difference equation (4.16) is by adding an increasing term to the numerical Hamiltonian. Let us consider the functional

$$u \in C(\overline{\Omega}) \longmapsto \widehat{\mathcal{R}}(u) := \delta^d \sum_{x \in \Omega_\delta} \left[ \widehat{H}_\alpha(x, D_\delta^+ u(x), D_\delta^- u(x)) + \tau u(x) \right]^2,$$

for some  $\tau > 0$ . In this case, the first-order optimality condition is of the form

$$(A_{\alpha,\delta}(U) + \tau I_{\Omega_\delta})W = 0,$$

where  $I_{\Omega_\delta}$  is the identity operator in the space of grid functions on  $\Omega_\delta$ , and  $W$  is the grid function associated to the function  $x \mapsto w(x) := \widehat{H}_\alpha(x, D_\delta^+ u(x), D_\delta^- u(x)) + \tau u(x)$ .

Similar arguments to the ones in the proofs of Theorems 1 and 2 can be used to obtain a sufficient condition on the parameters  $\alpha, \delta$  and  $\tau$ , ensuring that the matrix associated to the linear operator  $A_{\alpha,\delta}(U) + \tau I_{\Omega_\delta}$  is positive definite, for any grid function  $U$  on  $\Omega_\delta = \delta\mathbb{Z} \cap \Omega$  with Lipschitz constant  $L$ . This in turn implies that, for any function  $u$  with Lipschitz constant  $L$ , if  $u$  is a critical point of  $\widehat{\mathcal{R}}(u)$  then  $u$  satisfies the finite-difference equation (4.16).

### 4.4 Time dependent problems

There is no difficulty in extending our analysis to the time-dependent case:

$$\begin{cases} \partial_t u + H(x, \nabla u) = 0 & \Omega \times (0, T), \\ u(x, t) = g(x) & \partial\Omega \times (0, T), \\ u(x, 0) = u_0(x) & \Omega, \end{cases} \quad (4.17)$$

with  $T \in (0, \infty]$ , initial data  $u_0 : \Omega \rightarrow \mathbb{R}$  and boundary data  $g : \Omega \rightarrow \mathbb{R}$ .

In this case, a suitable choice for the least squares approach is to use the following finite-difference scheme

$$u(x, t + \delta_t) = u(x, t) - \delta_t \widehat{H}_\alpha(x, D_{\delta_x}^+ u(x, t), D_{\delta_x}^- u(x, t)), \quad (4.18)$$

for some  $\delta_t, \delta_x, \alpha > 0$ , which combines an explicit Euler scheme for the time derivative and a Lax-Friedrichs numerical Hamiltonian.

The least square finite-difference functional associated to the above numerical scheme is

$$\mathcal{R}(u) := \int_0^T \int_\Omega \left[ u(x, t + \delta_t) - u(x, t) + \delta_t \widehat{H}_\alpha(x, D_{\delta_x}^+ u(x, t), D_{\delta_x}^- u(x, t)) \right]^2 dx, \quad (4.19)$$

and can be coupled with the initial and boundary data as

$$\mathcal{J}(u) := \mathcal{R}(u) + \gamma_b \int_0^T \int_{\partial\Omega} (u(x, t) - g(x))^2 dx + \gamma_0 \int_{\Omega} (u(x, 0) - u_0(x))^2 dx. \quad (4.20)$$

A similar analysis of the critical points can be carried out for the above functional. Again, the conclusion is that by taking  $\alpha$  and  $\delta_x$  sufficiently large, one can ensure that any critical point satisfies the finite-difference equation associated with the numerical scheme (4.18). In Section 5.2.2, we show some numerical experiments, where we apply our least squares approach to time evolution problems of the form (4.17).

## 5 Numerics

As discussed in the introduction, the purpose of formulating the numerical method for (1.1) as a minimisation problem is that one can approximate the solution using a Neural Network trained through stochastic gradient descent (SGD). To enhance converge to the viscosity solution, we use the residual of a consistent and monotone Lax-Friedrichs numerical Hamiltonian in the loss functional, which ensures that any global minimiser approximates a viscosity solution. Due to the use of stochastic gradient descent as optimisation method, it is of utmost importance that any critical point of the functional is a global minimiser. However, in view of our main results Theorem 1 and Theorem 2, we can only ensure this by considering a numerical Hamiltonian that incorporates enough numerical diffusion ( $\alpha$  and  $\delta$  big enough in (4.3) or (4.10)). The drawback is that the global minimiser of the resulting minimisation problem is an over-smoothed approximation of the actual viscosity solution. Next, we describe an algorithm to approximate the global minimiser of a Lax-Friedrichs finite-difference loss with small parameters  $\alpha$  and  $\delta$ . The idea is to first apply SGD with large values of  $\alpha$  and  $\delta$ , ensuring convergence to the global minimiser, and then decrease these parameters to carry on with more SGD iterations and refine the approximation of the solution.

### 5.1 The proposed algorithms

Let us consider any NN function  $\Phi : \bar{\Omega} \times \Theta \rightarrow \mathbb{R}$ , where  $\Theta \subset \mathbb{R}^P$  is the parameter space and  $P$  is the number of parameters. We define the parameterized family of functions

$$\mathcal{F} := \{x \mapsto \Phi(x; \theta) : \theta \in \Theta\} \subset C(\bar{\Omega}). \quad (5.1)$$

Our numerical solution of (1.1) will be a function of the form  $u(x) = \Phi(x; \theta^*)$ , where  $\theta^* \in \Theta$  is obtained by minimising the function

$$\theta \mapsto \mathcal{J}(\Phi(\cdot; \theta)), \quad (5.2)$$

and  $\mathcal{J}$  is defined in (4.15) (or in (4.20) for time-dependent Hamilton-Jacobi equations). The minimisation algorithm to obtain  $\theta^*$  is a version of SGD in which, at every iteration, the functional  $\mathcal{J}$  in (4.15) is approximated by a Monte Carlo approximation of the integrals.

Let  $\mathcal{D}_0$ ,  $\mathcal{D}_{b_1}$ , and  $\mathcal{D}_{b_2}$  be the chosen probability distributions over  $\Omega$ ,  $\partial\Omega$ , and  $\Gamma$  respectively. Our algorithms are built on the typical stochastic gradient descent algorithm:

$$\theta_{j+1} = \theta_j - \eta_j \nabla_{\theta} \tilde{\mathcal{J}}(\Phi(\cdot, \theta_j)), \quad (5.3)$$

with

$$\begin{aligned} \tilde{\mathcal{J}} &:= \tilde{\mathcal{L}} + \tilde{\mathcal{R}}, \\ \tilde{\mathcal{L}}(\Phi(\cdot; \theta); \gamma_1, \gamma_2) &:= \frac{\gamma_1}{N_{b_1}} \sum_{x \in X_{b_1}} (\Phi(x; \theta) - g(x))^2 + \frac{\gamma_2}{N_{b_2}} \sum_{x \in X_{b_2}} (\Phi(x; \theta) - h(x))^2, \\ \tilde{\mathcal{R}}(\Phi(\cdot; \theta)) &:= \frac{1}{N_0} \sum_{x \in X} \left[ \hat{H}_{\alpha}(x, D_{\delta}^{+} u(x), D_{\delta}^{-} u(x)) \right]^2. \end{aligned}$$

Here,  $X$  is a set consisting of  $N_0$  i.i.d. samplings from  $\mathcal{D}_0$ ,  $X_{b_1}$  contains  $N_{b_1}$  i.i.d. samples from  $\mathcal{D}_{b_1}$ , and  $X_{b_2}$  contains  $N_{b_2}$  i.i.d. samples from  $\mathcal{D}_{b_2}$ . In the Deep Learning community, the i.i.d. samples  $X \subset \Omega$ ,  $X_{b_1} \subset \partial\Omega$  and  $X_{b_2} \subset \Gamma$  are often referred to as *mini-batches*, and  $N_0$ ,  $N_{b_1}$  and  $N_{b_2}$  denote the batch-size for each mini-batch.

A possible choice for the probability distributions  $\mathcal{D}$ ,  $\mathcal{D}_{b_1}$  and  $\mathcal{D}_{b_2}$  are the uniform distributions over  $\Omega$ ,  $\partial\Omega$ , and  $\Gamma$  respectively. However, as we observe in our numerical experiments below, other distributions can be more efficient, especially in high-dimensional domains.

**Algorithm 1** SGD for Lax-Friedrichs finite-difference loss**Require:**  $\gamma_1, \gamma_2 > 0$ ,  $\{\eta_j\}_{j=0}^J \in (0, \infty)^J$ ,  $N_0, N_{b_1}, N_{b_2} \in \mathbb{N}$ ,  $\mathcal{D}_0 \in \mathcal{P}(\Omega)$ ,  $\mathcal{D}_{b_1} \in \mathcal{P}(\partial\Omega)$ , and  $\mathcal{D}_{b_2} \in \mathcal{P}(\Gamma)$ .**Input:**  $\theta_0 \in \Theta$  and  $\alpha, \delta > 0$ .**procedure** SGDLxF( $\theta_0, \alpha, \delta$ )     $j \leftarrow 0$     **while**  $j < J$  **do**         $X \leftarrow N_0$  i.i.d. samples from  $\mathcal{D}_0$          $X_{b_1} \leftarrow N_{b_1}$  i.i.d. from  $\mathcal{D}_{b_1}$          $X_{b_2} \leftarrow N_{b_2}$  i.i.d. from  $\mathcal{D}_{b_2}$          $\theta^{j+1} := \theta^j - \eta_j \left( \nabla_{\theta} \tilde{\mathcal{L}}(\Phi(\cdot; \theta^j); \gamma_1, \gamma_2) + \nabla_{\theta} \tilde{\mathcal{R}}(\Phi(\cdot; \theta^j)) \right)$          $j \leftarrow j + 1$     **end while**    **return**  $\theta^J$ **end procedure**

If the NN is initialised to be close to a global minimiser, then the gradient descent iterations will converge to a global minimiser. By restricting the parameters to a compact set, we can have an estimate of the Lipschitz constant  $L$ . We can choose  $\alpha := \alpha_0 > 0$  and  $\delta := \delta_0 > 0$  accordingly to meet the condition set in (4.8) for the Lax-Friedrichs numerical Hamiltonian  $\hat{H}_{\alpha}(x, D_{\delta}^{+}u(x), D_{\delta}^{-}u(x))$  from (4.1).

In view of Theorem 2, we can ensure that any critical point of

$$\mathcal{R}(u) = \mathcal{R}_{\alpha_0, \delta_0}(u) = \int_{\Omega} \left[ \hat{H}_{\alpha_0}(x, D_{\delta_0}^{+}u(x), D_{\delta_0}^{-}u(x)) \right]^2 dx$$

with Lipschitz constant  $L > 0$  satisfies

$$\hat{H}_{\alpha}(x, D_{\delta}^{+}u(x), D_{\delta}^{-}u(x)) = 0 \quad \text{for all } x \in \Omega. \quad (5.4)$$

Hence, the gradient descent iterations will converge to a function that solves (or approximately solves) the above equation. Then, we can reduce the hyper-parameters  $\alpha, \delta$  by choosing

$$0 < \alpha := \alpha_1 \lesssim \alpha_0 \quad \text{and} \quad 0 < \delta := \delta_1 \lesssim \delta_0$$

and continue with the gradient descent iterations applied to the new functional  $\mathcal{R}_{\alpha_1, \delta_1}(u)$ . Due to the continuity of the critical points of  $\mathcal{R}(\cdot)$ , and of the solutions of (5.4) with respect to  $\alpha$  and  $\delta$ , we can ensure that, by initializing the NN close to a global minimiser of  $\mathcal{R}_{\alpha_0, \delta_0}(u)$ , the iterations will converge to a global minimiser of  $\mathcal{R}_{\alpha_1, \delta_1}(u)$ . This procedure can be iterated with a reduction schedule for  $\alpha$  and  $\delta$ . Every time we reduce the parameters  $\alpha$  and  $\delta$ , we obtain a function which is closer to the viscosity solution of (1.1). This procedure can be interpreted as an approximation of the vanishing viscosity method, in which the viscosity solution to the boundary value problem (1.1) is obtained as the limit  $\varepsilon \rightarrow 0^+$  of the viscous approximation (1.4).

**Algorithm 2** Optimisation for a Lax-Friedrichs finite-difference loss with a progressive refinement schedule**Require:**  $K \in \mathbb{N}$ ,  $L > 0$ ,  $\mathcal{F}$  as in (5.1) and  $\{(\alpha_k, \delta_k)\}_{k=0}^K \in (0, \infty)^{2K}$ .**Ensure:**  $(L, \alpha_0, \delta_0)$  satisfy (4.8) and  $\alpha_{k+1} < \alpha_k$  and  $\delta_{k+1} < \delta_k$  for all  $1 \leq k \leq K$ .    Initialise  $\theta_0 \in \Theta$  in a way that  $x \mapsto \Phi(x; \theta)$  has Lipschitz constant  $L$ .     $k \leftarrow 0$     **while**  $k < K$  **do**         $\theta_{k+1} := \text{SGDLxF}(\theta_k, \alpha_k, \delta_k)$  as defined in Algorithm 1         $k \leftarrow k + 1$     **end while**    **return**  $\theta_K$ **5.2 Computational experiments**

Next, we test the efficacy of our algorithm on various canonical HJ equations across different dimensions. We start with the eikonal equation posed on different domains (Section 5.2.1). Then, we consider a time-evolution HJ equation of the form (4.17) (Section 5.2.2). Finally, we consider HJ equations arising in control

problems and differential games associated to curvature constrained dynamics. In particular, we consider two problems associated to the Reeds-Shepp's car model: the shortest path to a given target (Section 5.2.3) and the pursuit evasion game (Section 5.2.4).

In all the experiments, we use a fully connected multi-layer perceptron (MLP) as NN architecture. For a chosen number of hidden layers  $\ell \in \mathbb{N}$  (NN depth) and a vector  $[d_1, \dots, d_\ell] \in \mathbb{N}^\ell$  representing the number of neurons in each hidden layer, this can be written as

$$\Phi(x; \theta) := W_\ell \sigma(W_{\ell-1} x \sigma(\dots \sigma(W_0 x + b_0)) + b_{\ell-1}) + b_\ell, \quad (5.5)$$

where  $\theta := \{(W_i, b_i)\}_{i=0}^\ell$  is the parameter of the NN. The matrices  $W_0 \in \mathbb{R}^{d_1 \times d}$ ,  $\{W_i\}_{i=1}^{\ell-1} \in \prod_{i=1}^{\ell-1} \mathbb{R}^{d_{i+1} \times d_i}$  and  $W_\ell \in \mathbb{R}^{d_\ell \times 1}$  are typically called weights, and the vectors  $\{b_i\}_{i=0}^{\ell-1} \in \prod_{i=0}^{\ell-1} \mathbb{R}^{d_{i+1}}$  and the scalar  $b_\ell \in \mathbb{R}$  are called biases. The function  $\sigma(\cdot) \in C(\mathbb{R}; \mathbb{R}^+)$  defined as  $\sigma(s) := \max\{0, s\}$  is the activation function, which acts component wise on vectors.

The NN function can also be written as

$$\Phi(x; \theta) = W_\ell y_\ell + b_\ell, \quad \text{where} \quad \begin{cases} y_i = \sigma(W_{i-1} y_{i-1} + b_{i-1}), & \text{for } i = 1, \dots, \ell \\ y_0 = x. \end{cases}$$

In the experiments, we vary the number of hidden layers and the number of neurons per layer depending on the complexity of the problem. For each case, the NN architecture will be indicated in the experiment description. For instance, for the case of a fully connected MLP with three hidden layers, the architecture is denoted by  $[d_1, d_2, d_3]$ , where  $d_1, d_2$  and  $d_3$  represent the number of neurons in each hidden layer. For the problems in Sections (5.2.3) and (5.2.4), we consider a slightly different architecture, due to the fact that the problem's domain requires the solution to be  $2\pi$ -periodic with respect to some of the variables. This is achieved by considering a linear combination of trigonometric functions, for which the coefficients are given by MLPs as defined above.

We have not explored other NN architectures. Depending on the specific problem under consideration, the use of other NN architectures such as *ResNet* might improve the performance of the method, however, this is left for future research.

In order to test the accuracy of the numerical solutions computed by the proposed method, we consider various examples for which the viscosity solution is available in closed form. Namely, we consider the eikonal equation in simple domains such as a cube, a ball and an annulus, in different dimensions. The viscosity solution in this case corresponds to the distance function to the boundary, and can be easily computed for the three aforementioned domains. This function is used as a ground truth to evaluate the accuracy of solution provided by the trained NN.

We use two metrics to evaluate the accuracy: the Mean Square Error (MSE) and the  $L^\infty$ -error. These are defined respectively as

$$MSE(\Phi(\cdot; \theta)) := \frac{1}{|\Omega|} \int_{\Omega} |\Phi(x; \theta) - u(x)|^2 dx \quad \text{and} \quad E_\infty(\Phi(\cdot; \theta)) := \max_{x \in \Omega} |\Phi(x; \theta) - u(x)|, \quad (5.6)$$

where  $u \in C(\overline{\Omega})$  is the viscosity solution, which is used as ground truth.

Obviously, we cannot compute exactly the integral in (5.6), which is approximated by the Monte Carlo method. For some  $N \in \mathbb{N}$ , let us define

$$\widetilde{MSE}(\Phi(\cdot; \theta)) := \frac{1}{N} \sum_{i=1}^N |\Phi(x_i; \theta) - u(x_i)|^2 \quad (5.7)$$

$$\widetilde{E}_\infty(\Phi(\cdot; \theta)) := \max_{i=0, \dots, N} |\Phi(x_i; \theta) - u(x_i)|, \quad (5.8)$$

where  $\{x_1, \dots, x_N\} \subset \Omega$  is an i.i.d. uniform sampling in  $\Omega$ , and  $x_0 = (0, 0, \dots) \in \mathbb{R}^d$  is the origin. Note that to approximate the  $L^\infty$ -error we add the origin to the sampling. Of course this does not apply to the case when  $\Omega$  is an annulus. When  $\Omega$  is a cube or a ball, we observe that the highest error of the numerical solution is achieved near the origin. Therefore, especially when the dimension is high, adding this point to the sampling improves the approximation of the  $L^\infty$ -error. In all the experiments below, we took the sample size for the Monte Carlo approximation as  $N = 10^6$ .

In the following sections, the run times for the experiments are recorded from running our PyTorch implementation on a desktop Dell with Intel Core i7-10700 CPU at 2.90GHz×16 with 15.4 GiB of RAM memory. The code is available in the following link:

[https://github.com/carlosesteveyague/HamiltonJacobi\\_LeastSquares\\_LxF\\_NNs](https://github.com/carlosesteveyague/HamiltonJacobi_LeastSquares_LxF_NNs)

### 5.2.1 Eikonal equation

To illustrate the algorithm presented in section 5.1, we carry out some numerical experiments for the Eikonal equation in a  $d$ -dimensional domain

$$\begin{cases} |\nabla u(x)|^2 = 1, & x \in \Omega, \\ u(x) = 0, & x \in \partial\Omega. \end{cases} \quad (5.9)$$

Let us start with a simple example by considering the domain  $\Omega := (-3, 3)^d$ . The solution, in this case, corresponds to the distance function to the boundary of the  $d$ -dimensional cube and can be written as

$$u(x) = 3 - \|x\|_\infty, \quad \forall x \in (-3, 3)^d. \quad (5.10)$$

We shall use the explicit solution as a ground truth to evaluate the accuracy of the numerical approximations.

**The two-dimensional case ( $d = 2$ ).** We use Algorithm 2, with  $K = 5$ , to train a fully connected Neural Network with one hidden layer with 20 neurons. The parameters  $\alpha$  and  $\delta$  in each round/iteration are assigned according to the following schedules:

$$\alpha \in \{2.5, 2, 1.5, 1, 0.5\} \quad \text{and} \quad \delta \in \{0.75, 0.5, 0.3, 0.1, 0.05\}. \quad (5.11)$$

Observe that, after each round, both parameters  $\alpha$  and  $\delta$  are decreased. This is designed to progressively reduce the effect of the numerical viscosity to obtain higher fidelity in the approximate solution in the final round. In each round, we applied Algorithm 1 with batch size  $N_0 = 50$  for the collocation points sampled uniformly in  $\Omega$ , and  $N_{b_1} = 30$  for the boundary points, sampled uniformly in  $\partial\Omega$ . The number of SGD iterations in each of the five rounds is

$$J \in \{500, 500, 1000, 1500, 2000\}.$$

As  $\delta$  decreases, each collocation point influences a smaller portion of the domain, and hence, more iterations of SGD are needed to minimise the loss functional. The flexibility in using different values of  $\delta$  to control the domain of influence for a finite set of collocation points may be another argument supporting the use of a finite-difference-based loss function over the PDE residual, which would correspond to the limit  $\delta \rightarrow 0^+$ .

In Figure 2, we can see the numerical approximation provided by the NN, at initialisation, and after each of the five rounds in Algorithm 2. In Figure 3, we see the evolution throughout the rounds of the Mean Square Error and the  $L^\infty$ -error (see (5.7) and (5.8)) of the numerical solution with respect to the ground truth solution (5.10). The total run time to train the NN was 5 seconds on a CPU.

**Higher dimensional cases.** Next, we consider the same problem in dimensions  $d = 5$  and  $d = 8$ . In each experiment, we conduct 4 rounds of Algorithm 2, again with decreasing parameters  $\alpha$  and  $\delta$ . As we increase the dimension, we need to increase the complexity of the NN and the number of collocation points. Rather than increasing the batch sizes  $N_0$  and  $N_{b_1}$  in (5.3), we increase the number of iterations per round. We compared the performance of different NN architectures. In particular, we used 2- and 3-layer fully connected MLP, with varying number of neurons per layer.

See Table 1 for a summary of the numerical experiments (each column corresponds to an independent experiment). In all the experiments, we used a uniform distribution to sample the points in  $\Omega$  and  $\partial\Omega$  during the iterations of Algorithm 1. In Figure 4, we see the evolution of the MSE and the  $L^\infty$ -error throughout the application of Algorithm 2.

As mentioned in section 5.1, it is possible to enhance the accuracy of the numerical solution by decreasing the values of  $\alpha$  and  $\delta$  throughout the iterations of Algorithm 2. However, we observe that this does not always produce a more accurate approximation. See in Figure 4 and in Figure 7 below that the error is not monotonically decreasing throughout the iterations of Algorithm 2. This phenomenon can be attributed to the fact that for smaller values of  $\delta$ , each collocation point has a smaller domain of influence over the



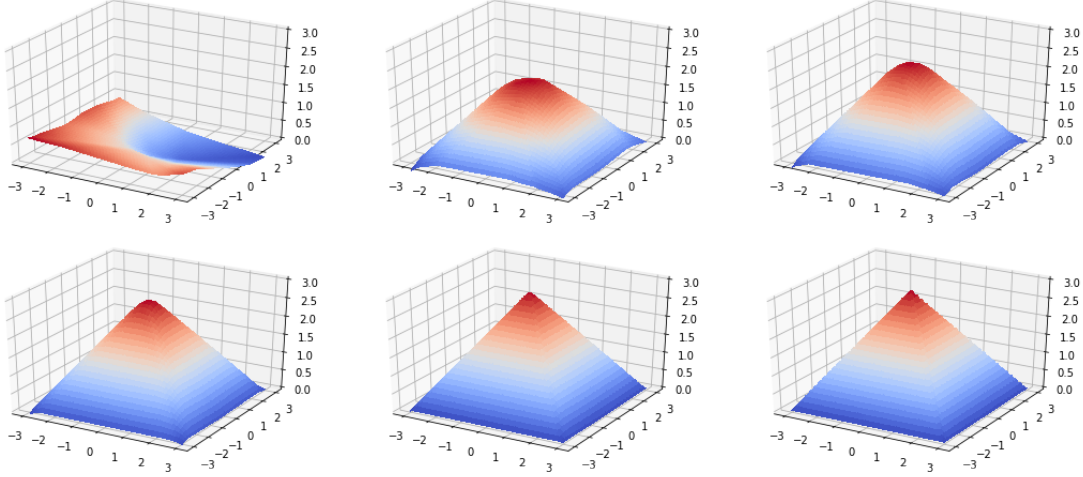


Figure 2: The numerical approximation of the Eikonal equation in  $\Omega = (-3, 3)^2$  constructed by Algorithm 1. The top-left plot corresponds to the NN at initialisation. Then, from left to right and from top to bottom, each plot corresponds to the approximation after every iteration. The values of  $\alpha$  and  $\delta$  are taken as in 5.11.

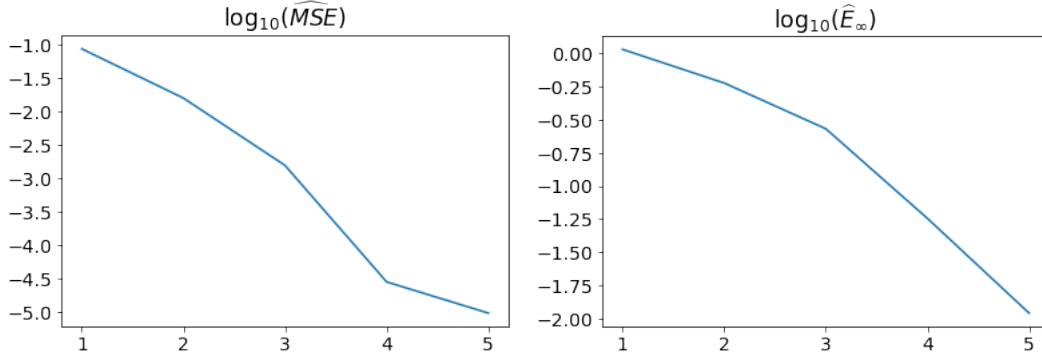


Figure 3: Evolution of the Mean Square Error and the  $L^{\infty}$ -Error after each round of Algorithm 2, for the Eikonal equation in  $(-3, 3)^2$ . The parameters  $\alpha$  and  $\delta$  in each of the five iterations are taken as in (5.11).

solution. This issue can be alleviated by increasing the number of collocation points, which is achieved in experiments 3 and 6 by increasing the number of SGD iterations.

Another way to understand this is by noting that, for smaller  $\delta$ , any grid with discretization step  $\delta$  contains more points, and hence, any functional associated to such discretization requires a larger number of collocation points to successfully approximate the minimiser.

We also observe that increasing the complexity of the NN also enhances the accuracy of the solution. In experiments 1 and 4 in table 1 we used a fully connected MLP with 2 hidden layers, whereas in experiments 2,3,5 and 6 we used an MLP with 3 hidden layers. In the evolution of the error shown in Figure 4, we observe that the improvement in accuracy given by the more complex NN is more noticeable for smaller values of  $\alpha$  and  $\delta$ . We recall that in this case, the minimiser of the functional is closer to the non-smooth viscosity solution. The same phenomenon can be observed in the experiments shown in Table 3 and Figure 7 for the eikonal equation in a  $d$ -dimensional annulus.

When the dimension is high, the sampling distribution used during the iterations of Algorithm 1 dramatically impacts the numerical solution. Let the domain  $\Omega$  be a  $d$ -dimensional ball. Sample points of the uniform distribution over  $\Omega$  with respect to the Lebesgue measure, will be closer to the boundary with higher probability. This is simply because the outer rings of the ball occupy a larger volume (of the order  $\sim r^{d-1}$ ). This ‘‘concentration’’ causes the accuracy near the centre of the ball to be relatively poor as compared to

Table 1: Summary of the numerical experiments for the eikonal equation in  $\Omega = (-3, 3)^d$  with  $d = 5, 8$ . In each experiment we applied 4 iterations of Algorithm 2 with decreasing values of  $\alpha$  and  $\delta$ , specifically,  $\alpha \in \{2.5, 2, 1, 0.5\}$  and  $\delta \in \{0.7, 0.3, 0.1, 0.02\}$ . See Figure 4 for the evolution of the MSE and the  $L^\infty$ -error after each iteration. In all the experiments, the batch size in the implementation of SGD in (5.3) is taken as  $N_0 = 200$  and  $N_{b_1} = 80$ .

Experiment	1	2	3	4	5	6
Dimension	5	5	5	8	8	8
Architecture	[30, 20]	[30, 20, 10]	[30, 20, 10]	[50, 40]	[40, 30, 20]	[40, 30, 20]
Iterations ( $\times 10^3$ )	{3, 3, 3, 3}	{3, 3, 3, 3}	{3, 4, 5, 8}	{6, 6, 6, 6}	{6, 6, 6, 6}	{6, 8, 10, 16}
MSE	0.014352	0.005000	0.000585	0.039507	0.013018	0.003277
$L^\infty$ -error	0.636471	0.394347	0.361236	0.707868	0.582976	0.613833
Runtime (s)	23	27	47	55	66	107

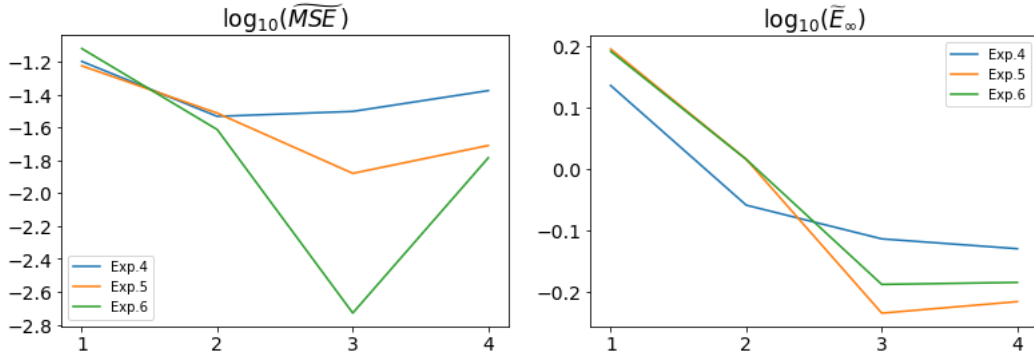


Figure 4: Evolution of the MSE (left) and the  $L^\infty$ -error (right) throughout the iterations of Algorithm 2, for the Experiments 4, 5 and 6 reported in Table 1. These correspond to the eikonal equation in an 8-dimensional cube.

the accuracy of the solution near the boundary. This issue can be overcome by using a different distribution for the collocation points. In the case when  $\Omega$  is a  $d$ -dimensional ball of radius  $R$ , one possibility is to use a radially uniform sampling, i.e.

$$X = rv, \quad \text{where } r \sim \text{Unif}(0, R) \text{ and } v \sim \text{Unif}(\mathbb{S}^{d-1}), \quad (5.12)$$

where  $\mathbb{S}^{d-1}$  denotes the  $(d-1)$ -dimensional unit sphere.

In Table 2, we see the summary of the numerical experiments for the Eikonal equation in a 10-dimensional ball of radius 6. Again, for each experiment we carried out 4 rounds of Algorithm 2. The evolution of the MSE and the  $L^\infty$ -error throughout the iterations of Algorithm 2 is shown in Figure 5. We observe that the accuracy of the numerical solution, in terms of MSE, is similar when using a uniform distribution or a radially uniform distribution to sample the collocation points in  $\Omega$ . See Table 2 and Figure 5 (left). However, if we look at the accuracy in terms of  $L^\infty$ -error, the accuracy is remarkably better when using the radially uniform sampling defined in (5.12). See Table 2 and Figure 5 (right). This is because, when using uniform sampling, most of the points are close to the boundary, and the accuracy near the centre of the ball is poorer. See Figure 6 for a representation of the numerical solution using different sampling distributions for the eikonal equation in the 10-dimensional ball  $\Omega = B_{10}(0, 6)$ . In the plot on the left, we used a uniform sampling for the collocation points during the optimisation algorithm, whereas in the plot at the right, we used the radially uniform sampling described in (5.12). In both cases, the plots represent the NN evaluated on a uniform grid of the two-dimensional cross-section  $B_2(0, 6) \times \{0\}$ <sup>8</sup>.

In Table 3, we can see the results of some numerical experiments for the solution of the Eikonal equation in an annulus of dimension  $d = 5$  and 10, with inner radius 2 and outer radius 6, i.e.

$$\Omega := \{x \in \mathbb{R}^d : 2 < |x| < 6\}.$$

Table 2: Summary of the numerical experiments for the eikonal equation in  $\Omega = B_{10}(0,6)$ , i.e. the 10-dimensional ball of radius 6. In each experiment we applied 4 iterations of Algorithm 2 with decreasing values of  $\alpha$  and  $\delta$ , specifically,  $\alpha \in \{2.5, 2, 1, 0\}$  and  $\delta \in \{0.7, 0.3, 0.1, 0.01\}$ . See Figure 5 for the evolution of the MSE and the  $L^\infty$ -error after each iteration. In all the experiments, the batch size in the implementation of SGD in (5.3) is taken as  $N_0 = 200$  and  $N_{b_1} = 80$ .

Experiment	1	2	3	4	5	6
Dimension	10	10	10	10	10	10
Distribution	Unif.	Unif.	Unif.	Rad.	Rad.	Rad.
Architecture	[40, 30]	[40, 30, 20]	[40, 30, 20]	[40, 30]	[40, 30, 20]	[40, 30, 20]
Iterations ( $\times 10^3$ )	{3, 3, 3, 3}	{3, 3, 3, 3}	{3, 5, 8, 12}	{3, 3, 3, 3}	{3, 3, 3, 3}	{3, 5, 8, 12}
MSE	0.012584	0.016928	0.007021	0.015622	0.016313	0.009513
$L^\infty$ -error	2.227512	2.439947	2.317906	0.598769	0.735229	0.604165
Runtime (s)	34	39	93	35	47	91

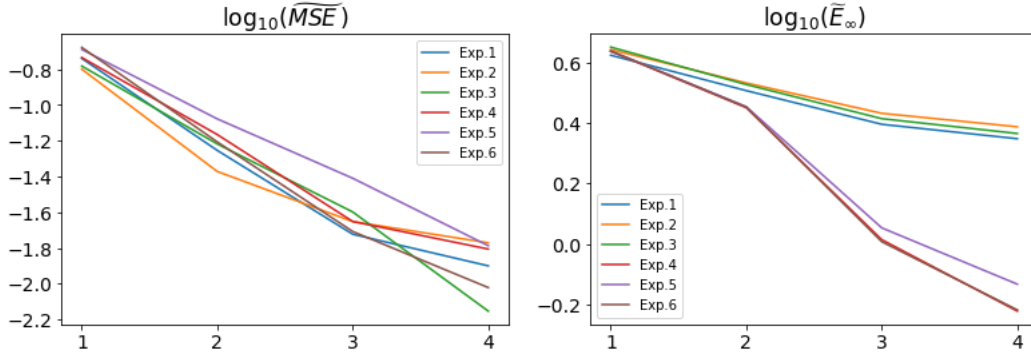


Figure 5: Evolution of the MSE (left) and the  $L^\infty$ -error (right) throughout the iterations of Algorithm 2, for the experiments reported in Table 2. These correspond to the eikonal equation in an 10-dimensional ball. We see that the use of a radially uniform distribution for the collocation points (experiments 4,5 and 6) improves the accuracy in terms of  $L^\infty$ -error.

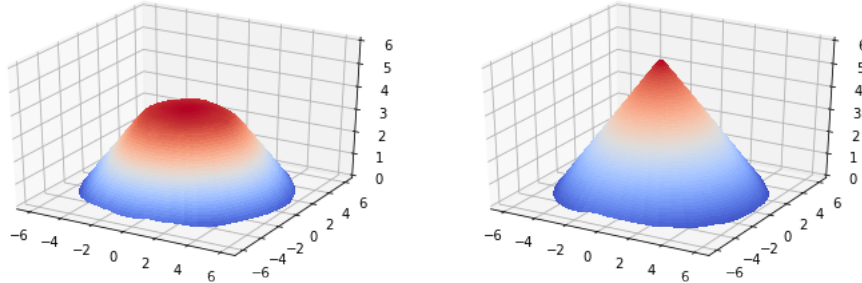


Figure 6: The numerical solution for the eikonal equation in  $\Omega = B_{10}(0,6) \subset \mathbb{R}^{10}$ , evaluated on a uniform grid of the two-dimensional cross-section  $B_2(0,6) \times \{0\}^8$ . In the figure at the left, a uniform distribution over  $\Omega$  has been used in Algorithm 1, whereas in the figure at the right, we used the radially uniform sampling defined in 5.12.

Table 3: Summary of the numerical experiments for the eikonal equation in  $\Omega = \{x \in \mathbb{R}^d : 2 < |x| < 6\}$  with  $d = 5, 10$ , i.e. the  $d$ -dimensional annulus with inner and outer radii 2 and 6 respectively. In each experiment we applied 4 iterations of Algorithm 2 with decreasing values of  $\alpha$  and  $\delta$ , specifically,  $\alpha \in \{2.5, 2, 1, 0.5\}$  and  $\delta \in \{0.7, 0.3, 0.1, 0.05\}$ . See Figure 7 for the evolution of the MSE and the  $L^\infty$ -error after each iteration. In all the experiments, the batch size in the implementation of SGD in (5.3) is taken as  $N_0 = 200$  and  $N_{b_1} = 80$ .

Experiment	1	2	3	4	5	6
Dimension	5	5	5	10	10	10
Distribution	Rad.	Rad.	Rad.	Rad.	Rad.	Rad.
Architecture	[40, 40]	[40, 40, 30]	[40, 40, 30]	[60, 60]	[60, 60, 40]	[60, 60, 40]
Iterations ( $\times 10^3$ )	{3, 3, 3, 3}	{3, 3, 3, 3}	{3, 5, 8, 12}	{6, 6, 6, 6}	{6, 6, 6, 6}	{6, 8, 12, 20}
MSE	0.011290	0.008826	0.002166	0.018800	0.035535	0.005379
$L^\infty$ -error	0.556805	0.367744	0.259248	0.687382	0.743850	0.383458
Runtime (s)	25	32	77	69	89	173

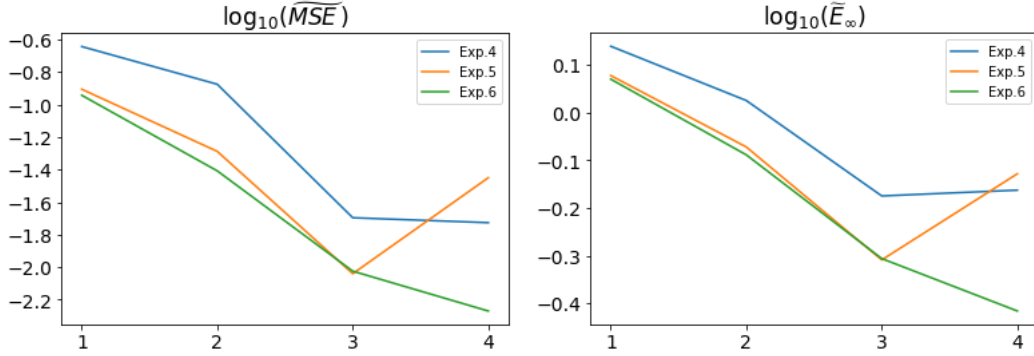


Figure 7: Evolution of the MSE (left) and the  $L^\infty$ -error (right) throughout the iterations of Algorithm 2, for the experiments 4,5 and 6 reported in Table 3. These correspond to the Eikonal equation in a 10-dimensional annulus. The final increase of errors in Experiment 5 reflects the fact that more SGD iterations is needed (compare with Experiment 6).

We applied 4 rounds of Algorithm 2 with decreasing values of  $\alpha$  and  $\delta$ . See Figure 7 for the evolution of the MSE and the  $L^\infty$ -error of the solution after each iteration. Comparing the settings for Experiments 5 and 6, the only difference is that Experiment 6 employed more SGD iterations in Algorithm 1. We see that to achieve smaller errors, the number of SGD iterations should increase as  $\delta$  decreases. This phenomenon might be attributed to the fact that, since discretization step is smaller, each collocation point has a smaller domain of influence. See Figure 8 for a representation of the numerical solution in a central cross-section of the domain.

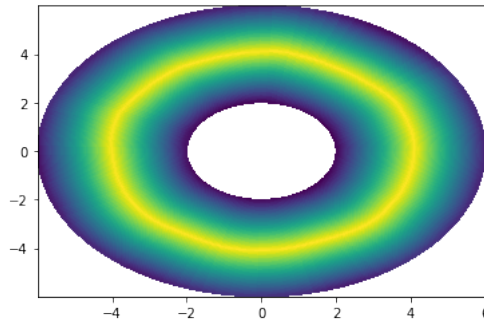


Figure 8: Cross-section of the numerical solution provided by the trained NN from experiment 6 in Table 3. The NN approximates the viscosity solution of the Eikonal equation in a 10-dimensional annulus.

Table 4: Summary of the experiments for time-dependent problems in dimension  $d = 2$  and  $d = 5$ . We used the NN architecture defined in (5.5) with  $\ell = 3$ , and architecture  $[50, 50, 50]$  and  $[200, 200, 200]$  respectively.

$d$	Architecture	$\alpha$	$\delta_x$	$\delta_t$	$N_0$	$N_{b_1}$	SGD iter.	$\mathcal{R}(u)$	$\mathcal{L}(u)$	Runtime (s)
2	[50,50,50]	2.5	0.5	0.05	40	40	5000	0.0205	0.0025	10
		2	0.3	0.03	80	40	5000	0.0247	0.0017	10
		1.5	0.2	0.05	120	40	5000	0.0258	0.0019	11
		1	0.1	0.01	200	40	8000	0.0262	0.0013	19
5	[200,200,200]	2.5	0.5	0.05	250	200	20000	0.0484	0.0111	238
		2	0.3	0.03	250	200	20000	0.0303	0.0033	242
		1.5	0.2	0.02	250	200	20000	0.0362	0.0037	244
		1	0.1	0.01	250	200	50000	0.0160	0.0025	609

### 5.2.2 Time-dependent problems

As mentioned in Section 4.4, our method can be applied to time-evolution Hamilton-Jacobi equations of the form (4.17). Here, we consider the initial value problem (4.17), in the domain  $\Omega := \mathbb{R}^d \times (0, \infty)$  with Hamiltonian

$$H(x, p) := \frac{|p|^2}{2} + \frac{|x|^2}{2}, \quad (x, p) \in \mathbb{R}^d \times \mathbb{R}^d,$$

and initial condition

$$u_0(x) = \frac{1}{2} (\langle x, Ax \rangle - 1),$$

where  $A = \text{diag}(4/25, 1, 1, \dots)$ . This example is taken from Example 2 in [6].

We consider the bounded domain  $\Omega := (-3, 3)^d \times (0, 1/2)$ , and minimize the functional

$$\mathcal{J}(u) := \mathcal{R}(u) + \gamma_0 \int_{\Omega} (u(x, 0) - u_0(x))^2 dx,$$

where  $\mathcal{R}(u)$  is defined as in (4.19). Note that we do not use supervised data for the entire boundary of  $\Omega$ . We only prescribe the initial condition on  $(-3, 3)^d \times \{0\}$ . However, due to the convexity of Hamiltonian with respect to  $p$  and of the initial condition  $u_0(\cdot)$ , the characteristic curves starting outside  $(-3, 3)^d$  never enter in  $(-3, 3)^d$ . This implies that the viscosity solution in  $(-3, 3)^d \times (0, T)$  is uniquely determined by the initial condition in  $(-3, 3)^d$ , i.e. the initial value problem

$$\begin{cases} \partial_t u + H(x, \nabla u) = 0 & (x, t) \in (-3, 3)^d \times (0, 1/2) \\ u(x, 0) = u_0(x) & x \in (-3, 3)^d \end{cases} \quad (5.13)$$

has a unique solution. Then, by choosing a finite-difference functional  $\mathcal{R}(u)$  such that any critical point approximates a viscosity solution, one can deduce that any critical point of  $\mathcal{J}(u)$  approximates the unique viscosity solution to the initial value problem (5.13).

We run two experiments with  $d = 2$  and with  $d = 5$ , in which the viscosity solution of (5.13) is approximated by a three-layer NN with 50 and 150 neurons per layer respectively. We run 4 iterations of Algorithm 2 with decreasing values of  $\alpha$  and  $\delta$  for each experiment. The results are reported in Table 4. Figure 9 shows the evolution of the 0-level set of the approximated solution for the two-dimensional case (left) and for the five-dimensional case (right).

### 5.2.3 Shortest path to a target for a Reeds-Shepp's car

Here, we consider an optimal control problem for a dynamical system with curvature constraints. In particular, we consider the Reeds and Shepp's car model [24], which can move backwards and forward with a limited turning radius. The pose of the car is represented by  $(x, y, \omega) \in \mathbb{R}^2 \times \mathbb{T}_{[0, 2\pi)}$ , where  $(x, y)$  represents the spatial position of the centre of mass of the car, and  $\omega$  represents its orientation angle. Here,  $\mathbb{T}_{[0, 2\pi)}$  denotes the one-dimensional flat torus of length  $2\pi$ . The optimal control problem involves steering the car to the origin  $(x, y) = 0$  from the given initial position  $(x_0, y_0, \omega_0)$  in the shortest possible time.

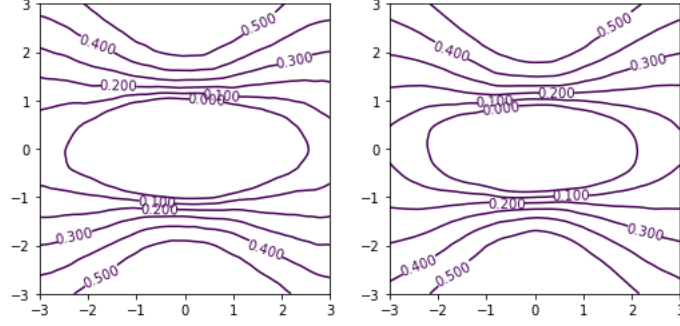


Figure 9: Two numerical solutions to the time-dependent problem, in dimension  $d = 2$  (left) and  $d = 5$  (right), defined in Section 5.2.2. In the plots, the zero-level sets of the approximate solutions,  $\{x \in \mathbb{R}^d : \Phi(x, t; \theta) = 0\}$ , are depicted for  $t = 0, 0.1, 0.2, 0.3, 0.4$  and  $0.5$ . The label for the curves reveal the corresponding values of  $t$ . In the 5-dimensional case (right), the plot represents the central cross-section of the domain  $(-3, 3)^2 \times \{0\}^3$ . See Table 4 for a summary of the experiments.

Denoting by  $t \mapsto (x(t), y(t), \omega(t)) \in \mathbb{R}^2 \times \mathbb{T}_{[0, 2\pi)}$  the trajectory of the car, the dynamics are given by the following ODE:

$$\begin{cases} \dot{x}(t) = \sigma a(t) \cos \omega(t) \\ \dot{y}(t) = \sigma a(t) \sin \omega(t) \\ \dot{\omega}(t) = \frac{b(t)}{\rho} \\ x(0) = x_0, y(0) = y_0, \omega(0) = \omega_0, \end{cases} \quad (5.14)$$

where  $\sigma > 0$  is the maximum speed of the car,  $\rho > 0$  is the inverse of the angular velocity of the car (the turning radius is therefore  $\sigma\rho$ ) and  $(x_0, y_0, \omega_0) \in \mathbb{R}^2 \times \mathbb{T}_{[0, 2\pi)}$  is the initial pose of the car. The time dependent functions  $a(\cdot), b(\cdot) : [0, \infty) \rightarrow [-1, 1]$  are the controls of the car.

Given the dynamics of the car, the Hamiltonian associated with the shortest path problem is given by

$$H(x, y, \omega, \nabla u) = \sigma |\partial_x u \cos \omega + \partial_y u \sin \omega| + \frac{1}{\rho} |\partial_\omega u| - 1,$$

where  $\nabla u = (\partial_x u, \partial_y u, \partial_\omega u)$  represents the gradient of  $u : \mathbb{R}^2 \times \mathbb{T}_{[0, 2\pi)} \rightarrow \mathbb{R}$  with respect to the pose of the car. We consider the target to be the ball of radius  $r = 0.2$  centred at the origin. Since our framework applies to bounded domains, we set  $R = 5$ , and define the domain

$$\Omega := \mathbb{A}_{r, R} \times \mathbb{T}_{[0, 2\pi)},$$

where  $\mathbb{A}_{r, R}$  denotes the two-dimensional annulus with inner radius  $r$  and outer radius  $R$

$$\mathbb{A}_{r, R} := \{(x, y) \in \mathbb{R}^2 : r < \sqrt{x^2 + y^2} < R\}. \quad (5.15)$$

As for the boundary conditions, we set 0 on the inner boundary of the annulus and  $R$  on the outer boundary. Hence, the resulting boundary value problem reads as

$$\begin{cases} H(x, y, \omega, \nabla u) = 0 & (x, y, \omega) \in \mathbb{A}_{r, R} \times \mathbb{T}_{[0, 2\pi)} \\ u(x, y, \omega) = 0 & (x, y, \omega) \in \{\sqrt{x^2 + y^2} = r\} \times \mathbb{T}_{[0, 2\pi)} \\ u(x, y, \omega) = R & (x, y, \omega) \in \{\sqrt{x^2 + y^2} = R\} \times \mathbb{T}_{[0, 2\pi)}. \end{cases} \quad (5.16)$$

We used our approach to approximate the viscosity solution of the above boundary value problem using a NN. Since the solution  $u(x, y, \omega)$  is  $2\pi$ -periodic with respect to  $\omega$ , we considered a parameterised family of functions of the form

$$\Phi(x, y, \omega; \theta) = \sum_{n=0}^{10} \phi(x, y; \theta_n^{(1)}) \cos(n\omega) + \sum_{m=1}^{10} \phi(x, y; \theta_m^{(2)}) \sin(m\omega),$$

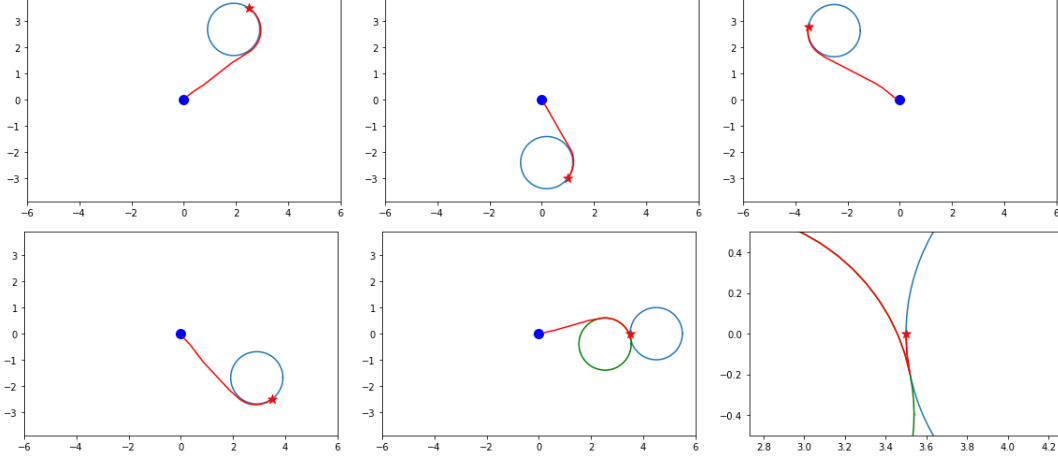


Figure 10: Five sample trajectories for the Reeds-Shepp's car, obtained using Neural Network approximating the viscosity solution of (5.16). The underlying optimal control problem is the shortest path problem to the origin (represented by the blue dot), subject to the curvature-constrained dynamics in (5.14). The red star represents the initial position of the car, and the blue circle represents the turning circumference from the initial position and orientation of the car. The bottom left figure is the fifth trajectory, zoomed-in around the initial position. The car maneuvers to find a shorter path to the target.

where the function  $\phi(\cdot, \cdot; \theta) : \mathbb{R}^2 \rightarrow \mathbb{R}$  is a three-layer fully connected NN with 60 neurons in each hidden layer. We trained the NN for three rounds of Algorithm 2, using the following values for the parameters  $\alpha$  and  $\delta$ :

$$\alpha \in \{2.5, 2.5, 2.5\} \quad \text{and} \quad \delta \in \{0.75, 0.6, 0.3\}.$$

In each application of Algorithm 1, we run 3000 iterations of stochastic gradient descent, using  $N_{b_1} = 100$  boundary points for the boundary data, and in each of the three rounds, we took  $N = [800, 1000, 1200]$  as number of collocation points to approximate the finite-difference loss. The time it took to train the NN was 90 seconds on a CPU. Figure 10 shows some trajectories obtained by the trained Neural Network.

#### 5.2.4 Pursuit-evasion game with Reeds-Shepp's cars

As an example of applying our method to a Hamilton-Jacobi equation arising from differential game theory, we consider the pursuit-evasion game for two players that move according to Reeds and Shepp's car model (5.14). Given the initial poses for the Evader and the Pursuer, represented by

$$(x_e, y_e, \omega_e) \in \mathbb{R}^2 \times \mathbb{T}_{[0, 2\pi)} \quad \text{and} \quad (x_p, y_p, \omega_p) \in \mathbb{R}^2 \times \mathbb{T}_{[0, 2\pi)},$$

we consider the game in which the Pursuer's goal is to intercept the Evader in the shortest possible time, and the Evader's goal is to delay the interception for as long as possible.

Since the position of the game only depends on the relative position between the players, we introduce the variables  $X = x_e - x_p$  and  $Y = y_e - y_p$ . The vector  $(X, Y)$  represents the vector joining the Evader with the Pursuer. The position of the game is therefore represented by  $(X, Y, \omega_e, \omega_p) \in \mathbb{R}^2 \times \mathbb{T}_{[1, 2\pi)}^2$ . In view of the dynamics of the two cars in (5.14), we can write down the dynamics for the evolution of the game as

$$\begin{cases} \dot{X}(t) = \sigma_e a_e(t) \cos \omega_e(t) - \sigma_p a_p(t) \cos \omega_p(t) \\ \dot{Y}(t) = \sigma_e a_e(t) \sin \omega_e(t) - \sigma_p a_p(t) \sin \omega_p(t) \\ \dot{\omega}_e(t) = \frac{b_e(t)}{\rho_e}, \quad \dot{\omega}_p(t) = \frac{b_p(t)}{\rho_p} \\ X(0) = x_e - x_p, \quad Y(0) = y_e - y_p, \quad \omega_e(0) = \omega_e, \quad \omega_p(0) = \omega_p, \end{cases} \quad (5.17)$$

where  $\sigma_e$  and  $\sigma_p$  represent the maximum velocities for the Evader and the Pursuer, respectively, and  $\rho_e$  and  $\rho_p$  represent the inverse of their angular velocity (the turning radius for the evader and the pursuer is  $\sigma_e \rho_e$  and  $\sigma_p \rho_p$  respectively). The functions  $a_e(\cdot), a_p(\cdot) : [0, \infty) \rightarrow [-1, 1]$  are the controls for the velocities of the players, and  $b_e(\cdot), b_p(\cdot) : [0, \infty) \rightarrow [-1, 1]$  are the controls for the direction.

In this case, we define the domain of the game as

$$\Omega := \mathbb{A}_{r,R} \times \mathbb{T}_{[0,2\pi)}^2,$$

with  $r = 0.2$ ,  $R = 4$ , where  $\mathbb{A}_{r,R}$  is the two-dimensional annulus defined in (5.15), and  $\mathbb{T}_{[0,2\pi)}^2$  is the two-dimensional flat torus with side-length  $2\pi$ . Recall that the position of the game is represented by the vector joining the players  $(X, Y) = (x_e - x_p, y_e - y_p) \in \mathbb{R}^2$  and the orientation angle of the players  $(\omega_e, \omega_p) \in \mathbb{T}_{[0,2\pi)}^2$ . The target for the Pursuer is the inner boundary of the annulus  $\mathbb{A}_{r,R}$ , where we set zero boundary condition. The target for the Evader is the outer boundary, where we set the boundary condition equal to 10.

In view of the dynamics of the game (5.17), and since the Pursuer is minimizing the output of the game and the Evader is maximizing it, we can derive the Hamiltonian associated with the game, which reads as

$$H(X, Y, \omega_e, \omega_p, \nabla u) := \sigma_p |\partial_X u \cos \omega_p + \partial_Y u \sin \omega_p| + \frac{1}{\rho_p} |\partial_{\omega_p} u| - \sigma_e |\partial_X u \cos \omega_e + \partial_Y u \sin \omega_e| - \frac{1}{\rho_e} |\partial_{\omega_e} u|,$$

where, for a function  $u : \Omega \rightarrow \mathbb{R}$  defined on the game domain,  $\nabla u = (\partial_X u, \partial_Y u, \partial_{\omega_e} u, \partial_{\omega_p} u)$  denotes the gradient of  $u$  with respect to the position of the game. The Hamilton-Jacobi-Isaacs equation associated to the game reads as follows:

$$\begin{cases} H(X, Y, \omega_e, \omega_p, \nabla u) = 0 & (X, Y, \omega_e, \omega_p) \in \mathbb{A}_{r,R} \times \mathbb{T}_{[0,2\pi)}^2 \\ u(x, y, \omega) = 0 & (x, y, \omega) \in \{\sqrt{X^2 + Y^2} = r\} \times \mathbb{T}_{[0,2\pi)} \\ u(x, y, \omega) = R & (x, y, \omega) \in \{\sqrt{X^2 + Y^2} = R\} \times \mathbb{T}_{[0,2\pi)}. \end{cases} \quad (5.18)$$

The viscosity solution of this boundary value problem characterises the value of the game and can be used to characterise the optimal feedback strategies for the players as

$$a_p(X, Y, \omega_e, \omega_p) = -\operatorname{sgn}(\partial_X u \cos \omega_p + \partial_Y u \sin \omega_p), \quad b_p(X, Y, \omega_e, \omega_p) = -\operatorname{sgn}(\partial_{\omega_p} u) \quad (5.19)$$

for the Pursuer, and

$$a_e(X, Y, \omega_e, \omega_p) = \operatorname{sgn}(\partial_X u \cos \omega_e + \partial_Y u \sin \omega_e), \quad b_e(X, Y, \omega_e, \omega_p) = \operatorname{sgn}(\partial_{\omega_e} u) \quad (5.20)$$

for the Evader.

For different values of the players' velocities  $(\sigma_e, \rho_e)$  and  $(\sigma_p, \rho_p)$ , we used our approach to approximate the viscosity solution of (5.18) using a NN. Similarly to the previous example, since the solution  $u(X, Y, \omega_e, \omega_p)$  is  $2\pi$ -periodic with respect to  $\omega_e$  and  $\omega_p$ , we considered a parameterised family of functions of the form

$$\begin{aligned} \Phi(X, Y, \omega_e, \omega_p; \theta) &= \sum_{n=0}^4 \phi(X, Y; \theta_n^{(1)}) \cos(n\omega_e) + \sum_{m=1}^4 \phi(X, Y; \theta_m^{(2)}) \sin(m\omega_e) \\ &\quad + \sum_{n=0}^4 \phi(X, Y; \theta_n^{(3)}) \cos(n\omega_p) + \sum_{m=1}^4 \phi(X, Y; \theta_m^{(4)}) \sin(m\omega_p) \end{aligned}$$

where the function  $\phi(\cdot, \cdot; \theta) : \mathbb{R}^2 \rightarrow \mathbb{R}$  is a three-layer fully connected NN with 80 neurons in each hidden layer. We trained the NN for three rounds of Algorithm 2, using the following values for the parameters  $\alpha$  and  $\delta$ :

$$\alpha \in \{2.5, 2, 1.5\} \quad \text{and} \quad \delta \in \{0.7, 0.5, 0.3\}.$$

In each application of Algorithm 1, we run 3000 iterations of stochastic gradient descent, using  $N_{b_1} = 100$  points for the boundary data, and  $N = 800$  collocation points to approximate the least-squares finite-difference loss. The running time to train each NN was 120 seconds on a CPU. In Figure 11, each sample trajectory of the game is computed according to (5.19) and (5.20), with a trained NN approximating the value function  $u$ . In the first example, the Pursuer moves faster than the Evader ( $\sigma_p > \sigma_e$ ), but the Evader has a higher angular velocity ( $1/\rho_e > 1/\rho_p$ ). The plot at the right represents the evolution of the distance between the players throughout the game. We see oscillatory behaviour due to the turns that the Evader performs for not being intercepted. Near the maxima of the curve, we see that the distance increases abruptly before it starts decreasing. This is due to the small maneuver of the Pursuer (similar to last example in Figure 10) allowing to change the direction faster. In the second example, we see a trajectory in which both players have the same angular velocity, but the pursuer moves faster. Hence, the turning radius of the Evader is smaller ( $\sigma_e \rho_e < \sigma_p \rho_p$ ). In this case, the game enters in a loop. Finally, in the third example, we see a trajectory in which the pursuer moves faster, and both players have the same turning radius ( $\sigma_e \rho_e = \sigma_p \rho_p$ ). In this case, the Pursuer has a clear advantage over the Evader, and interception occurs in a short time interval.



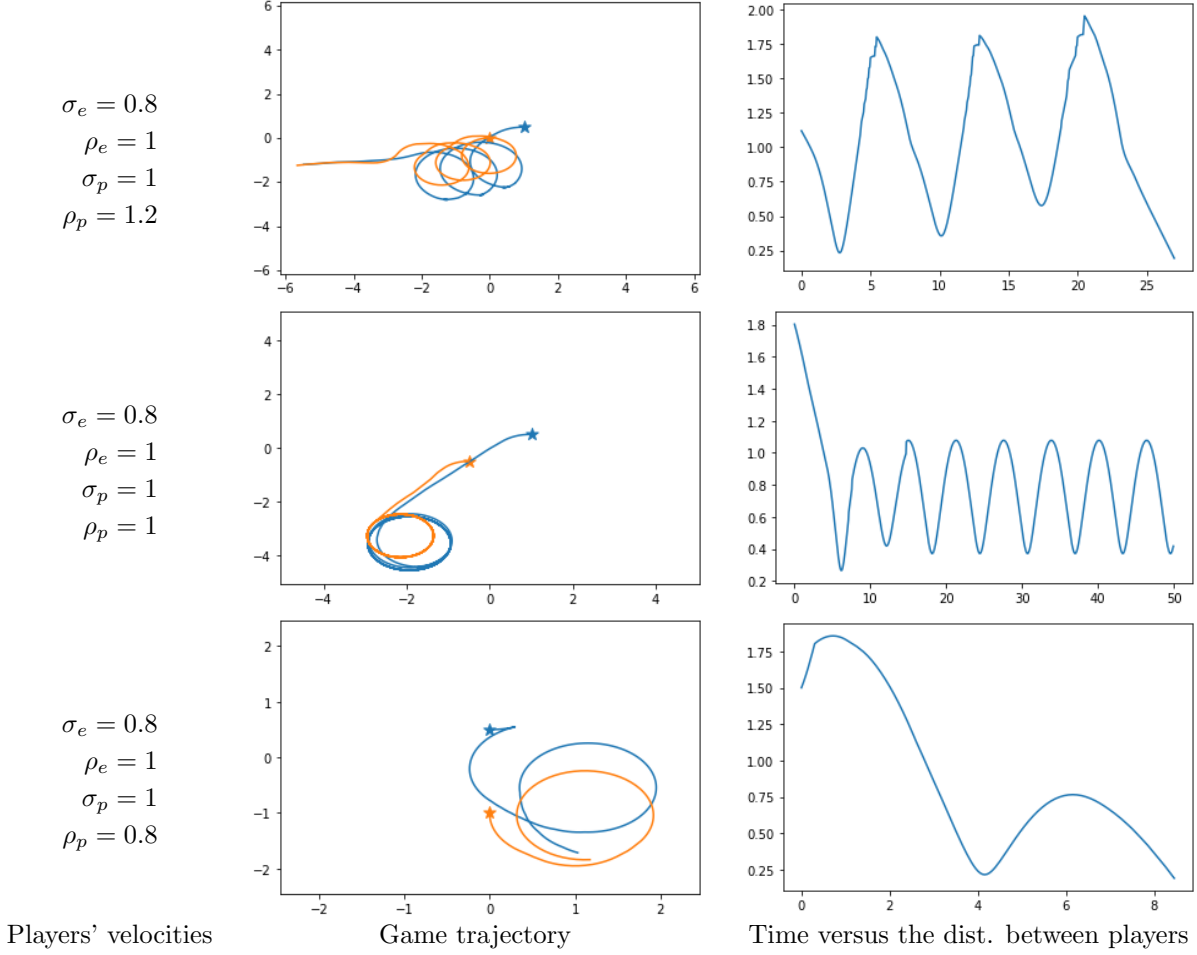


Figure 11: Three trajectories of the Pursuit Evasion game with Reeds-Shepp's cars discussed in Section 5.2.4. We consider different velocity parameters for the players (left) and different initial positions shown by the stars.

## 6 Proofs of the main results

### 6.1 Notation and preliminaries

In view of Theorems 1 and 2 and Corollary 1, in this section, we only consider the  $d$ -dimensional cube  $\Omega := (0, 1)^d$ . For any  $N \in \mathbb{N}$ , fix  $\delta = 1/N$ , and consider the uniform Cartesian grids of the domains  $\bar{\Omega}$  and  $\Omega$ , given by

$$\bar{\Omega}_\delta := \delta\mathbb{Z}^d \cap \bar{\Omega} = \{x_\beta := \delta\beta : \beta \in \{0, 1, \dots, N\}^d\} \quad (6.1)$$

$$\Omega_\delta := \delta\mathbb{Z}^d \cap \Omega = \{x_\beta := \delta\beta : \beta \in \{1, \dots, N-1\}^d\} \quad (6.2)$$

From now on, we will use the multi-index notation  $\beta := (\beta_1, \dots, \beta_d) \in \{0, 1, \dots, N\}^d$ . Furthermore, we denote by  $\{e_i\}_{i=1}^d$  the canonical basis of  $\mathbb{R}^d$ , so that  $x_{\beta+e_i} = x_\beta + \delta e_i$  and  $x_{\beta-e_i} = x_\beta - \delta e_i$ . We also introduce the index domains

$$\bar{\mathfrak{B}} := \{0, \dots, N\}^d \quad \text{and} \quad \mathfrak{B} := \{1, \dots, N-1\}^d. \quad (6.3)$$

Then, we can write  $\bar{\Omega}_\delta = \{x_\beta : \beta \in \bar{\mathfrak{B}}\}$  and  $\Omega_\delta = \{x_\beta : \beta \in \mathfrak{B}\}$ .

For a given a function  $u \in C(\bar{\Omega})$ , let us denote by  $U$  the grid function associated to  $u$  on the grid  $\bar{\Omega}_\delta$ , i.e.

$$U := \{U_\beta = u(x_\beta) : \beta \in \bar{\mathfrak{B}}\}.$$

Using the above notation, we can write the functional  $\widehat{\mathcal{R}}(u)$  as

$$\begin{aligned}\widehat{\mathcal{R}}(u) &= \delta^d \sum_{x \in \Omega_\delta} \left[ \widehat{H}_\alpha(x, D_\delta^+ u(x), D_\delta^- u(x)) \right]^2 \\ &= \delta^d \sum_{x \in \Omega_\delta} \left[ H \left( x, \frac{D_\delta^+ u(x) + D_\delta^- u(x)}{2} \right) - \alpha \sum_{i=1}^d \left( \frac{D_\delta^+ u(x) - D_\delta^- u(x)}{2} \right)_i \right]^2 \\ &= \delta^d \sum_{\beta \in \mathfrak{B}} \left[ H(x_\beta, D_\delta U_\beta) - \alpha \sum_{i=1}^d D_{\delta,i}^2 U_\beta \right]^2 =: F(U),\end{aligned}\tag{6.4}$$

where, for any  $\beta \in \mathfrak{B}$ ,  $D_\delta U_\beta$  denotes the centred finite-difference approximation of the gradient, i.e.

$$D_\delta U_\beta = \left( \frac{U_{\beta+e_1} - U_{\beta-e_1}}{2\delta}, \dots, \frac{U_{\beta+e_d} - U_{\beta-e_d}}{2\delta} \right) \in \mathbb{R}^d,\tag{6.5}$$

and, for any  $i \in \{1, \dots, d\}$ ,  $D_{\delta,i}^2 U_\beta$  is given by

$$D_{\delta,i}^2 U_\beta = \frac{U_{\beta+e_i} + U_{\beta-e_i} - 2U_\beta}{2\delta}.\tag{6.6}$$

In view of the assumption (1.3), the functional  $U \mapsto F(U)$  defined in (6.4) is differentiable in the space of grid functions on  $\overline{\Omega}_\delta$ . The main step in the proof of Theorem 1 is to verify that if  $\nabla F(U) = 0$ , then

$$H(x_\beta, D_\delta U_\beta) - \alpha \sum_{i=1}^d D_{\delta,i}^2 U_\beta = 0, \quad \forall \beta \in \mathfrak{B}.$$

In the next lemma, we compute the partial derivatives of  $F(U)$  with respect to  $U_\beta$ , for all  $\beta \in \mathfrak{B}$ .

**Lemma 1.** *Let  $H$  satisfy (1.3),  $\alpha > 0$  and, for any  $N \in \mathbb{N}$  and  $\delta = 1/N$ , consider the grid  $\overline{\Omega}_\delta$  as in (6.1), and the index domains  $\overline{\mathfrak{B}}$  and  $\mathfrak{B}$  as in (6.3). Let  $F(U)$  be defined as in (6.4) for any grid function  $U$  on  $\overline{\Omega}_\delta$ . Then we have*

$$\partial_{U_\beta} F(U) = -\delta^{d-1} \left( \sum_{i=1}^d \left( V_{\beta+e_i}^{(i)} W_{\beta+e_i} - V_{\beta-e_i}^{(i)} W_{\beta-e_i} \right) + \alpha \sum_{i=1}^d (W_{\beta+e_i} + W_{\beta-e_i} - 2W_\beta) \right), \quad \forall \beta \in \mathfrak{B},$$

where

$$W_\beta := \begin{cases} H(x_\beta, D_\delta U_\beta) - \alpha \sum_{i=1}^d D_{\delta,i}^2 U_\beta, & \forall \beta \in \mathfrak{B}, \\ 0 & \forall \beta \in \overline{\mathfrak{B}} \setminus \mathfrak{B}, \end{cases}\tag{6.7}$$

and for all  $i \in \{1, \dots, d\}$ ,

$$V_\beta^{(i)} := \begin{cases} \partial_{p_i} H(x_\beta, D_\delta U_\beta), & \forall \beta \in \mathfrak{B} \\ 0 & \forall \beta \in \overline{\mathfrak{B}} \setminus \mathfrak{B}. \end{cases}\tag{6.8}$$

*Proof.* Note that, in view of the definition of  $F(U)$  in (6.4) and the definition of  $W = \{W_\beta\}_{\beta \in \overline{\mathfrak{B}}}$  in (6.7), we have

$$F(U) = \sum_{\beta \in \overline{\mathfrak{B}}} W_\beta^2.$$

For any  $\beta \in \mathfrak{B}$ , the term  $U_\beta$  appears only in the terms associated to the index  $\beta$  and the indexes  $\beta \pm e_i$  for all  $i \in \{1, \dots, d\}$ . Moreover, we note that, in view of (6.5), the term  $H(x_\beta, D_\delta U_\beta)$  is independent of  $U_\beta$ , and for any  $i$ , the terms  $H(x_{\beta \pm e_i}, D_\delta U_{\beta \pm e_i})$  depend on  $U_\beta$  only through the  $i$ -th component of the vector  $D_\delta U_{\beta \pm e_i}$ .

Hence, we can write  $\partial_{U_\beta} F(U)$  as

$$\begin{aligned} \partial_{U_\beta} F(U) &= -2\delta^d \alpha W_\beta \sum_{i=1}^d \partial_{U_\beta} (D_{\delta,i}^2 U_\beta) \\ &\quad + 2\delta^d \sum_{i=1}^d W_{\beta+e_i} \left( \underbrace{\partial_{p_i} H(x_{\beta+e_i}, D_\delta U_{\beta+e_i})}_{V_{\beta+e_i}^{(i)}} \partial_{U_\beta} (D_\delta U_{\beta+e_i})_i - \alpha \partial_{U_\beta} (D_{\delta,i}^2 U_{\beta+e_i}) \right) \\ &\quad + 2\delta^d \sum_{i=1}^d W_{\beta-e_i} \left( \underbrace{\partial_{p_i} H(x_{\beta-e_i}, D_\delta U_{\beta-e_i})}_{V_{\beta-e_i}^{(i)}} \partial_{U_\beta} (D_\delta U_{\beta-e_i})_i - \alpha \partial_{U_\beta} (D_{\delta,i}^2 U_{\beta-e_i}) \right). \end{aligned} \quad (6.9)$$

Using (6.6), we can compute

$$\partial_{U_\beta} (D_{\delta,i}^2 U_\beta) = \partial_{U_\beta} \left( \frac{U_{\beta+e_i} + U_{\beta-e_i} - 2U_\beta}{2\delta} \right) = -\frac{1}{\delta}.$$

Next, for any  $i \in \{1, \dots, d\}$  such that  $\beta + e_i \in \mathfrak{B}$  (note that the terms such that  $\beta + e_i \notin \mathfrak{B}$  do not matter since  $W_{\beta+e_i}$  would be zero), we can use (6.5) and (6.6) to compute

$$\begin{aligned} \partial_{U_\beta} (D_\delta U_{\beta+e_i})_i &= \partial_{U_\beta} \left( \frac{U_{\beta+2e_i} - U_\beta}{2\delta} \right) = -\frac{1}{2\delta}, \\ \partial_{U_\beta} (D_{\delta,i}^2 U_{\beta+e_i}) &= \partial_{U_\beta} \left( \frac{U_{\beta+2e_i} + U_\beta - 2U_{\beta+e_i}}{2\delta} \right) = \frac{1}{2\delta}. \end{aligned}$$

Similarly, for any  $i \in \{1, \dots, d\}$  such that  $\beta - e_i \in \mathfrak{B}$ , we can compute

$$\begin{aligned} \partial_{U_\beta} (D_\delta U_{\beta-e_i})_i &= \partial_{U_\beta} \left( \frac{U_\beta - U_{\beta-2e_i}}{2\delta} \right) = \frac{1}{2\delta}, \\ \partial_{U_\beta} (D_{\delta,i}^2 U_{\beta-e_i}) &= \partial_{U_\beta} \left( \frac{U_\beta + U_{\beta-2e_i} - 2U_{\beta-e_i}}{2\delta} \right) = \frac{1}{2\delta}. \end{aligned}$$

By plugging all these values in (6.9), we obtain

$$\partial_{U_\beta} F(U) = \delta^{d-1} \sum_{i=1}^d 2\alpha W_\beta + \delta^{d-1} \sum_{i=1}^d \left( -V_{\beta+e_i}^{(i)} - \alpha \right) W_{\beta+e_i} + \delta^{d-1} \sum_{i=1}^d \left( V_{\beta-e_i}^{(i)} - \alpha \right) W_{\beta-e_i},$$

and the conclusion follows by regrouping the terms in the above sum.  $\square$

## 6.2 Proof of Theorem 1 and Corollary 1

We are now in position to carry out the proof of Theorem 1, which consists of two steps:

- i. First we prove that if  $u \in C(\bar{\Omega})$  is a critical point of  $\hat{\mathcal{R}}(\cdot)$ , then the associated grid function  $U$  on  $\bar{\Omega}_\delta$  satisfies  $\nabla F(U) = 0$ , where  $F(U)$  is given by (6.4).
- ii. Then, we use Lemma 1 to prove that if  $u$  is  $L$ -Lipschitz, and  $\alpha$  and  $\delta$  satisfy (4.8), then  $\nabla F(U) = 0$  implies that  $\hat{H}_\alpha(x, D_\delta^+ u(x), D_\delta^- u(x)) = 0$  for all  $x \in \Omega_\delta$ .

*Proof. Step 1:* Let  $u \in C(\bar{\Omega})$ . If  $u$  is a critical point of  $\hat{\mathcal{R}}(\cdot)$ , then it must hold that

$$\lim_{\varepsilon \rightarrow 0} \frac{\hat{\mathcal{R}}(u + \varepsilon \phi) - \hat{\mathcal{R}}(u)}{\varepsilon} = 0, \quad \text{for any function } \phi \in C(\bar{\Omega}). \quad (6.10)$$

Now, for any grid function  $\Phi$  on  $\bar{\Omega}_\delta$ , let  $\phi \in C(\bar{\Omega})$  be a function such that  $\phi(x_\beta) = \Phi_\beta$  for all  $\beta \in \bar{\mathfrak{B}}$ . In other words, consider a continuous function  $\phi$  such that the associated grid function is  $\Phi$ . In view of (6.10), and using the function  $F(\cdot)$  as defined in (6.4), we deduce that

$$0 = \lim_{\varepsilon \rightarrow 0} \frac{\hat{\mathcal{R}}(u + \varepsilon \phi) - \hat{\mathcal{R}}(u)}{\varepsilon} = \lim_{\varepsilon \rightarrow 0} \frac{F(U + \varepsilon \Phi) - F(U)}{\varepsilon} = \nabla F(U) \cdot \Phi.$$

Since this holds for any grid function  $\Phi$ , we deduce that  $\nabla F(U) = 0$ .

Step 2: In view of Lemma 1, the equation  $\nabla F(U) = 0$  can be written as

$$-\delta^{d-1}(A_N(V) + \alpha\Delta_N)W = 0,$$

where  $W$  and  $V = (V^{(1)}, \dots, V^{(d)})$  are the grid functions on  $\Omega_\delta$  defined in the statement of Lemma 1, and  $A_N(V)$  and  $\Delta_N$  are linear operators on the space of grid functions on  $\Omega_\delta$ , defined below, in Lemmas 2 and 3 respectively. The conclusion of the proof follows after proving that the linear operator  $A_N(V) + \alpha\Delta_N$  is invertible, so the optimality condition  $\nabla F(U) = 0$  implies that  $W = 0$ , and hence,

$$\widehat{H}_\alpha(x_\beta, D_\delta^+ u(x_\beta), D_\delta^- u(x_\beta)) = H(x_\beta, D_\delta U_\beta) - \alpha \sum_{i=1}^d D_{\delta,i}^2 U_\beta = W_\beta = 0, \quad \forall \beta \in \mathfrak{B}.$$

Recall that, by the Definition (6.2),  $\Omega_\delta = \{x_\beta : \beta \in \mathfrak{B}\}$ . To prove that the operator  $A_N(V) + \alpha\Delta_N$  is invertible, it is enough to prove that

$$\underline{\sigma}(A_N(V) + \alpha\Delta_N) = \min_W \frac{\|(A_N(V) + \alpha\Delta_N)W\|_2}{\|W\|_2} > 0.$$

Note that  $\underline{\sigma}(A_N(V) + \alpha\Delta_N)$  is a lower bound for the modulus of the eigenvalues of  $A_N(V) + \alpha\Delta_N$ . Using Lemmas 2 and 3 below, we have that

$$\begin{aligned} \underline{\sigma}(A_N(V) + \alpha\Delta_N) &\geq \min_W \frac{\alpha\|\Delta_N W\|_2 - \|A_N(V)W\|_2}{\|W\|_2} \\ &\geq \min_W \frac{\alpha\|\Delta_N W\|_2}{\|W\|_2} - \max_W \frac{\|A_N(V)W\|_2}{\|W\|_2} \\ &\geq 4\alpha d \sin^2\left(\frac{\pi}{2}\delta\right) - 2dC_H(L). \end{aligned}$$

Hence, we deduce that  $\underline{\sigma}(A_N(V) + \alpha\Delta_N) > 0$  provided  $2\alpha \sin^2\left(\frac{\pi}{2}\delta\right) > C_H(L)$ , where  $C_H(L)$  is defined in the statement of Lemma 2.  $\square$

Next, we prove the two following lemmas, which are used, at the end of the proof of Theorem 1, to bound the spectrum of the operators  $A_N(V)$  and  $\Delta_N$ . Although these results might be known to the expert reader, we include them for completeness.

**Lemma 2.** *Let  $H$  satisfy (1.3), consider the domain  $\Omega = (0, 1)^d$  and, for any  $N \in \mathbb{N}$  and  $\delta = 1/N$ , let  $\overline{\Omega}_\delta$  be the grid defined in (6.1). For any function  $u \in C(\overline{\Omega})$  with Lipschitz constant  $L > 0$ , let  $U$  be the grid function associated to  $u$  on the grid  $\overline{\Omega}_\delta$ , and set  $V = (V^{(1)}, \dots, V^{(d)})$ , where for each  $i \in \{1, \dots, d\}$ ,  $V^{(i)}$  is the grid function on  $\overline{\Omega}_\delta$  defined by (6.8).*

*Then, the linear operator defined, for any grid function  $W$  on  $\overline{\Omega}_\delta$ , by*

$$A_N(V)W = \sum_{i=1}^d \left( V_{\beta+e_i}^{(i)} W_{\beta+e_i} - V_{\beta-e_i}^{(i)} W_{\beta-e_i} \right),$$

*satisfies*

$$\overline{\sigma}(A_N(V)) := \max_W \frac{\|A_N(V)W\|_2}{\|W\|_2} \leq 2dC_H(L),$$

*where  $C_H(L) = \max_{\substack{\|p\| \leq L \\ x \in \overline{\Omega}}} \|\nabla_p H(x, p)\|$ .*

*Proof.* Using the definition of  $V^{(i)}$  in (6.8) and the fact that  $u$  has Lipschitz constant  $L$ , it holds that

$$V_\beta^{(i)} \leq C_H(L), \quad \forall \beta \in \mathfrak{B} \text{ and } i \in \{1, \dots, d\}.$$

Then, in view of the definition of  $A_N(V)$ , it follows that

$$\overline{\sigma}(A_N(V)) \leq C_H(L)\overline{\sigma}(\overline{A}), \tag{6.11}$$

where  $\overline{A}$  is the linear operator, on the space of grid functions on  $\Omega_\delta$ , given by

$$\overline{A} = \sum_{i=1}^d A^{(i)},$$

with

$$\begin{aligned} A^{(1)} &= B \otimes I \otimes \cdots \otimes I \\ A^{(2)} &= I \otimes B \otimes \cdots \otimes I \\ &\vdots \\ A^{(d)} &= I \otimes I \otimes \cdots \otimes B, \end{aligned}$$

where  $I$  is the  $(N-1) \times (N-1)$  identity matrix, and  $B \in \mathbb{R}^{(N-1) \times (N-1)}$  is given by

$$B = \begin{bmatrix} 0 & 1 & & & \\ 1 & 0 & 1 & & \\ & 1 & 0 & 1 & \\ & & \ddots & \ddots & \ddots \\ & & & 1 & 0 & 1 \\ & & & & 1 & 0 \end{bmatrix}.$$

Finally, by Gershgorin Theorem, the largest eigenvalue of  $B$  is smaller or equal than 2, so we conclude that

$$\overline{\sigma}(\overline{A}) \leq \sum_{i=1}^d \overline{\sigma}(A^{(i)}) \leq 2d,$$

and the conclusion of the lemma follows from (6.11).  $\square$

**Lemma 3.** *Let  $N \in \mathbb{N}$ ,  $\delta = 1/N$ , and consider the grid  $\Omega_\delta$  as in (6.1) and the index domain  $\mathfrak{B}$  as in (6.3). The linear operator  $\Delta_N$ , defined for any grid function  $W$  on  $\Omega_\delta$  as*

$$\Delta_N W = \sum_{i=1}^d (W_{\beta+e_i} + W_{\beta-e_i} - 2W_\beta),$$

with  $W_{\beta \pm e_i} = 0$  whenever  $\beta \pm e_i \notin \mathfrak{B}$ , satisfies

$$\underline{\sigma}(\Delta_N) := \min_W \frac{\|\Delta_N W\|_2}{\|W\|_2} = 4d \sin^2\left(\frac{\pi}{2}\delta\right).$$

*Proof.* The operator  $\Delta_N$  is the Dirichlet Laplacian associated with the  $d$ -dimensional grid  $\Omega_\delta$ , and is a symmetric negative definite operator. Hence,  $\underline{\sigma}(\Delta_N)$  coincides with the smallest eigenvalue of  $-\Delta_N$ . We can write it as

$$-\Delta_N = -\sum_{i=1}^d \Delta_N^{(i)},$$

with

$$\begin{aligned} \Delta_N^{(1)} &= L_N \otimes I \otimes \cdots \otimes I \\ \Delta_N^{(2)} &= I \otimes L_N \otimes \cdots \otimes I \\ &\vdots \\ \Delta_N^{(d)} &= I \otimes I \otimes \cdots \otimes L_N, \end{aligned}$$

and where

$$L_N = \begin{bmatrix} -2 & 1 & & & \\ 1 & -2 & 1 & & \\ & 1 & -2 & 1 & \\ & & \ddots & \ddots & \ddots \\ & & & 1 & -2 & 1 \\ & & & & 1 & -2 \end{bmatrix} \in \mathbb{R}^{(N-1) \times (N-1)}.$$

Any eigenvector of  $-\Delta_N$  can be written as  $\Phi = \bigotimes_{i=1}^d \phi^{(i)}$ , where  $\phi^{(i)} \in \mathbb{R}^{N-1}$  is an eigenvector of  $-L_N$  with associated eigenvalue  $\Lambda = \sum_{i=1}^d \lambda^{(i)}$ , where each  $\lambda^{(i)}$  is the eigenvalue associated to  $\phi^{(i)}$ . Hence, the smallest eigenvalue of  $-\Delta_N$  is  $d\lambda_1$ , where  $\lambda_1$  is the smallest eigenvalue of  $-L_N$ . Since the latter is well-known to be  $\lambda_1 = 4 \sin^2\left(\frac{\pi}{2N}\right)$ , we conclude that

$$\sigma(\Delta_N) = d\lambda_1 = 4d \sin^2\left(\frac{\pi}{2N}\right) = 4d \sin^2\left(\frac{\pi}{2}\delta\right).$$

□

Next, we give the proof of Corollary 1. The proof is almost identical to that of Theorem 1, with the only difference being that one has to consider the functional's partial derivatives with respect to the boundary points.

*Proof of Corollary 1.* First, for any function  $u \in C(\bar{\Omega})$ , let us write the functional  $\widehat{\mathcal{J}}(u)$  as

$$\widehat{\mathcal{J}}(u) = F(U) + \gamma G(U),$$

where  $F(U)$  is defined as in (6.4), and  $G(U)$  is given by

$$G(U) := \delta^{d-1} \sum_{\beta \in \overline{\mathfrak{B}} \setminus \mathfrak{B}} (U_\beta - g(x_\beta))^2.$$

Here, we use the multi-index notation introduced in (6.3).

Using precisely the same argument as in step 1 in the proof of Theorem 1, we have that if  $u$  is a critical point of  $\widehat{\mathcal{J}}(u)$ , then it must hold that  $\nabla F(U) + \gamma \nabla G(U) = 0$ .

Since  $G(U)$  does not depend on  $U_\beta$  for any  $\beta \in \mathfrak{B}$ , we have that  $u$  being a critical point of  $\widehat{\mathcal{J}}(u)$  implies that

$$\partial_{U_\beta} F(U) = -\delta^{d-1} \left( \sum_{i=1}^d \left( V_{\beta+e_i}^{(i)} W_{\beta+e_i} - V_{\beta-e_i}^{(i)} W_{\beta-e_i} \right) + \alpha \sum_{i=1}^d (W_{\beta+e_i} + W_{\beta-e_i} - 2W_\beta) \right) = 0, \quad \forall \beta \in \mathfrak{B},$$

where  $W_\beta$  and  $V_\beta^{(i)}$  are given as in (6.7) and (6.8). Now, using the step 2 in the proof of Theorem 1, we obtain that, if (4.8) holds, then  $W_\beta = 0$  for all  $\beta \in \mathfrak{B}$ .

Since  $W_\beta = 0$  for all  $\beta \in \mathfrak{B}$ , we have that

$$\partial_{U_\beta} F(U) + \gamma \partial_{U_\beta} G(U) = \gamma \partial_{U_\beta} G(U) = 2\gamma \delta^{d-1} (U_\beta - g(x_\beta)), \quad \forall \beta \in \overline{\mathfrak{B}} \setminus \mathfrak{B}.$$

Hence,  $\partial_{U_\beta} F(U) + \gamma \partial_{U_\beta} G(U) = 0$  implies that  $U_\beta = g(x_\beta)$  for all  $\beta \in \overline{\mathfrak{B}} \setminus \mathfrak{B}$ . This, combined with  $W_\beta = 0$  for all  $\beta \in \mathfrak{B}$  concludes the proof. □

### 6.3 Proof of Theorem 2

The main idea of the proof is to re-write the functional  $\mathcal{R}(\cdot)$  in such a way that we can apply the conclusion of Theorem 1 for the discrete functional  $\widehat{\mathcal{R}}(\cdot)$ .

*Proof.* Let  $N \in \mathbb{N}$  and fix  $\delta = 1/(N-1)$ . The interval  $[0, 1]$  can be partitioned in  $N-1$  disjoint intervals as

$$[0, 1] = \left[0, \frac{1}{N-1}\right) \sqcup \left[\frac{1}{N-1}, \frac{2}{N-1}\right) \sqcup \dots \sqcup \left[\frac{N-2}{N-1}, 1\right) = \bigsqcup_{\beta \in \{1, \dots, N-1\}} (\delta\beta + [-\delta, 0)).$$

Hence, for any dimension  $d$ , we can write  $[0, 1]^d$  similarly as a disjoint union of  $(N-1)^d$  disjoint  $d$ -dimensional cubes as

$$[0, 1]^d = \bigsqcup_{\beta \in \mathfrak{B}} (\delta\beta + [-\delta, 0)^d), \quad \text{where } \mathfrak{B} := \{1, \dots, N-1\}^d.$$

Now, recalling that  $\Omega = (0, 1)^d$ , we can use this partition to write  $\mathcal{R}(u)$  defined in (4.10) as

$$\begin{aligned}\mathcal{R}(u) &= \sum_{\beta \in \mathfrak{B}} \int_{(-\delta, 0)^d} \left[ \hat{H}_\alpha(z - \delta\beta, D_\delta^+ u(z - \delta\beta), D_\delta^- u(z - \delta\beta)) \right]^2 dz \\ &= \int_{(-\delta, 0)^d} \sum_{\beta \in \mathfrak{B}} \left[ \hat{H}_\alpha(z - \delta\beta, D_\delta^+ u(z - \delta\beta), D_\delta^- u(z - \delta\beta)) \right]^2 dz \\ &= \int_{(-\delta, 0)^d} \hat{\mathcal{R}}(u; z) dz,\end{aligned}\tag{6.12}$$

where

$$\hat{\mathcal{R}}(u; z) := \sum_{x \in \Omega_\delta(z)} \left[ \hat{H}_\alpha(x, D_\delta^+ u(x), D_\delta^- u(x)) \right]^2,$$

with  $\Omega_\delta(z) := \{x_\beta = z + \delta\beta : \beta \in \mathfrak{B}\}$  for all  $z \in (0, 1)^d$ .

Note that  $\Omega_\delta(z)$  is simply a shift of the grid  $\Omega_\delta$  defined in (6.2). Hence, by virtue of Theorem 1, if  $u \in C(\bar{\Omega})$  is a critical point of  $\hat{\mathcal{R}}(u; z)$ , then  $\hat{H}_\alpha(x, D_\delta^+ u(x), D_\delta^- u(x)) = 0$  for all  $x \in \Omega_\delta(z)$ .

For any functions  $u, v \in C(\bar{\Omega})$ , and any  $z \in (0, 1)^d$ , let  $U(z)$  and  $V(z)$  be the grid functions of  $u$  and  $v$  associated to the grid  $\Omega_\delta(z)$ , i.e.

$$U(z) := \{u(x) : x \in \Omega_\delta(z)\}, \quad \text{and} \quad V(z) := \{v(x) : x \in \Omega_\delta(z)\}.$$

We also define, for any  $z \in (0, \delta)^d$ , the functional on the space of grid functions on  $\Omega_\delta(z)$  given by

$$F_z(U(z)) := \sum_{x \in \Omega_\delta(z)} \left[ \hat{H}_\alpha(x, D_\delta^+ u(x), D_\delta^- u(x)) \right]^2 = \hat{\mathcal{R}}(u; z).$$

If  $u \in C(\bar{\Omega})$  is a critical point of  $\mathcal{R}(\cdot)$ , then for any function  $v \in C(\bar{\Omega})$  it must hold that

$$\lim_{\varepsilon \rightarrow 0} \frac{\mathcal{R}(u + \varepsilon v) - \mathcal{R}(u)}{\varepsilon} = 0,$$

or equivalently, we can use (6.12) to write

$$\int_{(-\delta, 0)^d} \lim_{\varepsilon \rightarrow 0} \frac{\hat{\mathcal{R}}(u + \varepsilon v; z) - \hat{\mathcal{R}}(u; z)}{\varepsilon} dz = \int_{(-\delta, 0)^d} \nabla F_z(U(z)) \cdot V(z) dz = 0.$$

Since this holds for any function  $v \in C(\bar{\Omega})$ , we deduce that  $\nabla F_z(U(z))$  is identically 0 for all  $z \in (-\delta, 0)^d$ . Whence,  $u$  is a critical point of  $\hat{\mathcal{R}}(u; z)$  for all  $z$ , and the conclusion follows.  $\square$

## 7 Summary and perspectives

In this paper, we propose to solve the boundary value problems for a class of Hamilton-Jacobi equations using Deep Learning. Artificial neural networks are trained by typical gradient descent-based algorithms, optimizing for the least square problem defined by the residual of a consistent and monotone finite difference scheme for the equation. We analyze the critical points of the least square problem in the space of continuous functions and reveal conditions that guarantee the critical points being the unique viscosity solution of the problem. These conditions may involve the parameters of the chosen finite difference scheme or those coming from additional “supervised” data points. We demonstrated numerically that the proposed approach effectively solves Hamilton-Jacobi equations in higher dimensions under a favourable setup.

An important point is that artificial neural networks are used instead of grid functions. Thus, one may take advantage of neural networks’ approximation power for the smooth parts of a solution and the scaling property of Monte-Carlo sampling involved in the training procedure. Thus, under favourable conditions, it is reasonable to expect that the proposed approach would suffer less the so-called “curse of dimensionality” than the classical algorithms.

But during the training iterations, one must ensure that the (high dimensional) computational domain is sufficiently “covered” — enough to effectively follow the characteristics from the boundaries to everywhere in the domain and “monitor” how the monotone scheme resolves the collision of the characteristics. This is crucial for computing accurate approximation of the viscosity solutions.

In PINNs, it is common knowledge that the choice of collocation points can determine the success of the methods. This is also true for the proposed approach, given a limited training budget. In higher dimensions, due to the “concentration of measure” errors, the errors “deeper” in the interior of  $\Omega$  are significantly “discounted.” However, reducing the errors in the interior may be essential to constructing approximate solutions with the proper global structure (such as convexity). Therefore, uniform sampling (relative to the Lebesgue measure) in training or assigning additional “supervised” data may be sub-optimal. We plan to develop adaptive algorithms for the proposed approach in the near future.

We point out that it is possible to use high-resolution schemes. However, suppose a gradient descent-based optimization scheme that utilizes automatic differentiation is used. In that case, the chosen numerical scheme must be a differentiable function to the variables defined by the scheme’s stencil. This formerly precludes the use of higher order essentially non-oscillatory (ENO) schemes [22]. However, the weighted essentially oscillatory (WENO) schemes [16] can be considered.

Finally, we remark that the idea of using a convergent numerical method to form least square principles is not limited to only finite difference methods. It is possible to develop such an algorithm using the finite element methodology. In that case, we envision that during training, proper mesh refinement strategies may be involved to enhance error control.

## Acknowledgement

Tsai is partially supported by NSF grant DMS-2110895 and by Army Research Office Grant W911NF2320240.

## References

- [1] F. Bach. Breaking the curse of dimensionality with convex neural networks. *Journal of Machine Learning Research*, 18(19):1–53, 2017.
- [2] M. Bardi and I. Capuzzo-Dolcetta. *Optimal control and viscosity solutions of Hamilton-Jacobi-Bellman equations*. Birkhäuser Boston Inc., Boston, MA, 1997. With appendices by Maurizio Falcone and Pierpaolo Soravia.
- [3] G. Barles and P. E. Souganidis. Convergence of approximation schemes for fully nonlinear second order equations. *Asymptotic Anal.*, 4(3):271–283, 1991.
- [4] A. R. Barron. Universal approximation bounds for superpositions of a sigmoidal function. *IEEE Transactions on Information theory*, 39(3):930–945, 1993.
- [5] A. Borovykh, D. Kalise, A. Laignelet, and P. Parpas. Data-driven initialization of deep learning solvers for hamilton-jacobi-bellman pdes. *IFAC-PapersOnLine*, 55(30):168–173, 2022.
- [6] Y. T. Chow, J. Darbon, S. Osher, and W. Yin. Algorithm for overcoming the curse of dimensionality for state-dependent hamilton-jacobi equations. *Journal of Computational Physics*, 387:376–409, 2019.
- [7] M. G. Crandall, H. Ishii, and P.-L. Lions. User’s guide to viscosity solutions of second order partial differential equations. *Bulletin of the American mathematical society*, 27(1):1–67, 1992.
- [8] M. G. Crandall and P.-L. Lions. Viscosity solutions of Hamilton-Jacobi equations. *Trans. Amer. Math. Soc.*, 277(1):1–42, 1983.
- [9] M. G. Crandall and P.-L. Lions. Two approximations of solutions of Hamilton-Jacobi equations. *Mathematics of computation*, 43(167):1–19, 1984.
- [10] J. Cui, S. Liu, and H. Zhou. A supervised learning scheme for computing hamilton-jacobi equation via density coupling. *arXiv preprint arXiv:2401.15954*, 2024.
- [11] J. Darbon and S. Osher. Algorithms for overcoming the curse of dimensionality for certain hamilton-jacobi equations arising in control theory and elsewhere. *Research in the Mathematical Sciences*, 3(1):19, 2016.



- [12] S. Dolgov, D. Kalise, and K. K. Kunisch. Tensor decomposition methods for high-dimensional hamilton-jacobi-bellman equations. *SIAM Journal on Scientific Computing*, 43(3):A1625–A1650, 2021.
- [13] S. Dolgov, D. Kalise, and L. Saluzzi. Data-driven tensor train gradient cross approximation for hamilton-jacobi-bellman equations. *SIAM Journal on Scientific Computing*, 45(5):A2153–A2184, 2023.
- [14] J. Helmsen, E. Puckett, P. Colella, and M. Dorr. Two new methods for simulating photolithography development in 3d. In *SPIE 2726*, pages 253–261, 1996.
- [15] H. Ishii. Perron’s method for Hamilton-Jacobi equations. *Duke Mathematical Journal*, 55(2):369 – 384, 1987.
- [16] G.-S. Jiang and D. Peng. Weighted ENO schemes for Hamilton-Jacobi equations. *SIAM J. Sci. Comput.*, 21(6):2126–2143 (electronic), 2000.
- [17] D. Kalise and K. Kunisch. Polynomial approximation of high-dimensional hamilton-jacobi-bellman equations and applications to feedback control of semilinear parabolic pdes. *SIAM Journal on Scientific Computing*, 40(2):A629–A652, 2018.
- [18] H. P. Le, T. T. Le, and L. H. Nguyen. The carleman convexification method for hamilton-jacobi equations. *Computers & Mathematics with Applications*, 159:173–185, 2024.
- [19] K. L. Lim, R. Dutta, and M. Rotaru. Physics informed neural network using finite difference method. In *2022 IEEE International Conference on Systems, Man, and Cybernetics (SMC)*, pages 1828–1833, 2022.
- [20] T. Meng, W. Hao, S. Liu, S. J. Osher, and W. Li. Primal-dual hybrid gradient algorithms for computing time-implicit hamilton-jacobi equations. *arXiv preprint arXiv:2310.01605*, 2023.
- [21] T. Meng, S. Liu, W. Li, and S. Osher. A primal-dual hybrid gradient method for solving optimal control problems and the corresponding hamilton-jacobi pdes. *arXiv preprint arXiv:2403.02468*, 2024.
- [22] S. Osher and C.-W. Shu. High-order essentially nonoscillatory schemes for Hamilton-Jacobi equations. *SIAM J. Numer. Anal.*, 28(4):907–922, 1991.
- [23] M. Raissi, P. Perdikaris, and G. E. Karniadakis. Physics-informed neural networks: A deep learning framework for solving forward and inverse problems involving nonlinear partial differential equations. *Journal of Computational physics*, 378:686–707, 2019.
- [24] J. Reeds and L. Shepp. Optimal paths for a car that goes both forwards and backwards. *Pacific journal of mathematics*, 145(2):367–393, 1990.
- [25] J. Sethian. Fast marching level set methods for three dimensional photolithography development. In *SPIE 2726*, pages 261–272, 1996.
- [26] J. A. Sethian. *Level set methods and fast marching methods*. Cambridge University Press, Cambridge, second edition, 1999. Evolving interfaces in computational geometry, fluid mechanics, computer vision, and materials science.
- [27] R. Sharma and V. Shankar. Accelerated training of physics-informed neural networks (pinns) using meshless discretizations, 2023.
- [28] Z. Shen, H. Yang, and S. Zhang. Nonlinear approximation via compositions. *Neural Networks*, 119:74–84, 2019.
- [29] J. W. Siegel and J. Xu. Approximation rates for neural networks with general activation functions. *Neural Networks*, 128:313–321, 2020.
- [30] J. W. Siegel and J. Xu. Sharp bounds on the approximation rates, metric entropy, and n-widths of shallow neural networks. *Foundations of Computational Mathematics*, 24(2):481–537, 2024.
- [31] Y.-H. R. Tsai, L.-T. Cheng, S. Osher, and H.-K. Zhao. Fast sweeping methods for a class of Hamilton-Jacobi equations. *SIAM J. Numer. Anal.*, 41(2):673–699, 2003.
- [32] J. Tsitsiklis. Efficient algorithms for globally optimal trajectories. *IEEE Transactions on Automatic Control*, 40(9):1528–1538, 1995.
- [33] E. Weinan, C. Ma, and L. Wu. Barron spaces and the compositional function spaces for neural network models. *arXiv preprint arXiv:1906.08039*, 2019.
- [34] E. Weinan and S. Wojtowytsch. Representation formulas and pointwise properties for barron functions. *Calculus of Variations and Partial Differential Equations*, 61(2):46, 2022.

- [35] D. Yarotsky. Error bounds for approximations with deep relu networks. *Neural networks*, 94:103–114, 2017.
- [36] H. Zhao. A fast sweeping method for eikonal equations. *Mathematics of computation*, 74(250):603–627, 2005.